Photonic crystal fibres and their applications in the nonlinear regime

Stone, James

Award date:
2009

Awarding institution:
University of Bath

PHOTONIC CRYSTAL FIBRES AND THEIR APPLICATIONS IN THE NONLINEAR REGIME

James Morgan Stone

A thesis submitted for the degree of Doctor of Philosophy

University of Bath
Department of Physics

April 2009

for dad

Contents

Acknowledgements

I'd like to wholeheartedly thank... sorry Greg, to thank wholeheartedly:

Those who took the time to proof read various stages of this thesis: Greg (who's made reading this an altogether more pleasant experience), Brian and Berwyn.

All the members of the CPPM, including those who have come and gone during my time, in particular those with which I worked closely: Feng, Tim, David, Greg, Dimitry, Andrei, Alan, Steve, Chun Le, William and Rodrigo.

Matt, for modifying, and Dimitry, for writing, nonlinear codes.

All my collaborators from other universities: the Applied Optics and Photonics Group at Heriot-Watt University; John Travers, Roy Taylor and the rest of the FOG at Imperial College.

John Clowes, Fianium and their lawyers.

Finally, and most of all, Jonathan, for everything.

Overview

This thesis presents several advances in the technology and applications of photonic crystal fibres achieved over the last three years. Chapters 1 and 2 give the background material important to understand the results presented in chapters 3, 4 and 5.

In chapter 1, linear properties of optical fibres are described. This chapter focuses particularly on how the engineering of the cladding structure of solid core photonic crystal fibres can be used to vary the fibre properties, most importantly the group index and dispersion. Propagation in all-solid photonic bandgap fibres is also discussed in terms of the anti-resonant reflecting optical waveguide model.

Chapter 2 introduces the nonlinear optical effects that are important to understand the work presented in chapters 4 and 5.

In chapter 3, a method to reduce bend losses in all-solid photonic bandgap fibres is outlined. The reduction of these losses is achieved by redesigning the high-index inclusions in the cladding structure to suppress cladding modes that strongly couple to the fundamental core-guided mode when the fibre is bent.

In chapter 4, a method of tapering photonic crystal fibres in order to decrease the dispersion along their length is described. The tapers are used to

compress solitons via adiabatic soliton compression and a combination of adiabatic soliton compression and soliton effect compression, achieving a factor of 15 compression of a transform-limited pulse to below 50 fs.

Chapter 5 describes how engineering the cladding structure of photonic crystal fibres can be used to generate shorter frequencies in supercontinuum generation. The method by which this achieved is experimentally verified and then exploited to generate a continuum incorporating the entire visible spectrum using low cost, low maintenance pump sources.

Chapter 1

Optical fibres

1.1 Introduction

This chapter is intended to summarise important background material necessary to understand the work presented in chapters 3, 4 and 5. It is neither intended to to be complete, or even logically arranged, but to provide a useful reference point to the reader. Important properties of conventional optical fibres and photonic crystal fibres are discussed, with the notable exception of nonlinear optics (important for chapters 4 and 5), this is discussed in a devoted chapter: chapter 2. The interested reader may like to consider several review articles for further reading [1, 2].

Since the possibility of guiding light through optical fibres was first explored in the middle of the twentieth century, the field has expanded, driven on principally by the desire for fast communications networks. This has led not only to the development of low-loss long haul telecommunications fibres, but has also driven research into fibre lasers and amplifiers. One result of this has been reliable, relatively maintenance-free components used in today's vast

global communications network. The uses for optical fibres and fibre lasers are not limited to communications, however, and find numerous applications—particularly in medicine and for fundamental research into the nature of light. In this chapter, we will give an overview of properties of optical fibres that are important for understanding the rest of this thesis, and introduce the particular properties of photonic crystal fibres, the main subject of this work. Principal subjects discussed are the linear propagation of light in optical fibres, dispersion, loss etc. and a method of understanding photonic bandgap guidance using the anti-resonant reflecting optical waveguide (ARROW) model.

Conventional optical fibres guide light through total internal reflection (TIR) [3]. When light is incident on a boundary of two materials of different refractive indices, some light is reflected and some is refracted. When light in a high-index material approaches the boundary with a material of lower refractive index approaching parallel, known as the critical angle, the refracted light travels along the boundary. At greater angles than this to the normal to the boundary all the light is reflected back into the material. Optical fibres in their simplest form achieve guidance through TIR by consisting of two regions: a high-index core and a cladding region of slightly lower refractive index (fig. 1.1a) enabling TIR along their length. Both materials used for the core and cladding are generally fused silica with the addition of different dopants to change the refractive index slightly [4]. Long haul communications fibres consist of a germanium-doped core and pure silica cladding. The germanium doping gives a slightly higher refractive index than that of pure silica. Other dopants which raise the refractive index of silica are aluminum, phosphorus and nitrogen, whereas fluorine and boron lower the refractive index. The index-lowering dopants can be used to form low index claddings around cores formed from pure silica.

In 1996, a new kind of optical fibre was reported which, instead of having a cladding region formed from one glass, had a cladding region comprising an array of microscopic air holes running along the fibre length [1, 2, 5]. This became known as photonic crystal fibre (PCF) and is represented schematically

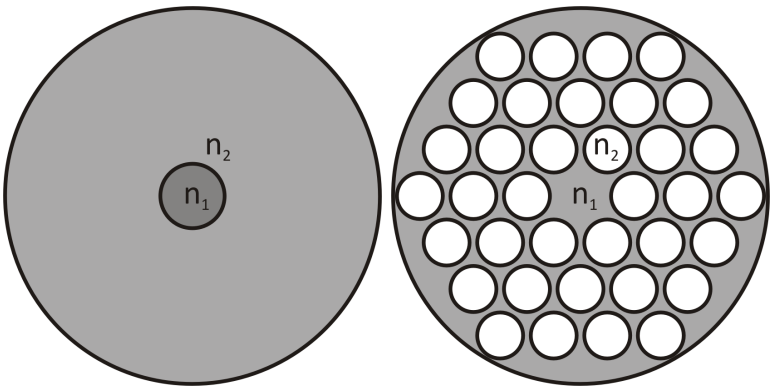

Figure 1.1: Schematic representations of cross sections through (a) a conventional optical fibre and (b) a solid core photonic crystal fibre. In (a) the darker grey region represents a core consisting of a glass of slightly higher refractive index than that of the cladding region shown in a lighter grey. In (b) the white regions in the cladding represent an array of air holes running the length of the fibre.

in fig. 1.1b. The array of air holes in the cladding gives PCFs significantly different guidance properties from conventional TIR guiding fibres. This is because the index contrast between the core (typically pure silica) and the cladding can be varied by altering the size of the cladding air holes, which changes the effective refractive index of the cladding region. Control of the effective refractive index allows significant engineering of fibre properties such as dispersion and nonlinearity. PCFs can also display properties which are not observed in conventional fibres. For example, with certain hole size to hole separation (pitch, Λ) ratios, they can only ever support the fundamental guided mode, regardless of wavelength [6, 7].

The 'solid core' PCFs described above are not the only type of PCF (fig. 1.2). Another class of PCF has a different guidance mechanism altogether from TIR, known as photonic bandgap guidance [8,9]. For this mechanism, it is no longer a requirement that the core have a higher refractive index than the cladding. This allows fibres to be fabricated with air cores. Hollow core photonic crystal fibres (HC-PCFs), and a similar class of fibre with again a different guidance

mechanism known as kagome fibres [10–12], have allowed gas-laser interactions over far longer lengths than are achievable in free space [10, 13, 14]. The photonic bandgap fibres (PBGFs) that are most important to the work in this thesis are all-solid photonic bandgap fibres (AS-PBGFs) [15, 16]. These are fabricated with a cladding array of two different glasses with different refractive indices, rather than with glass and air. Historically these have suffered from high loss when the fibre is bent. In chapter 3.8, an improved AS-PBGF is presented with a cladding structure engineered specifically to reduce bend losses.

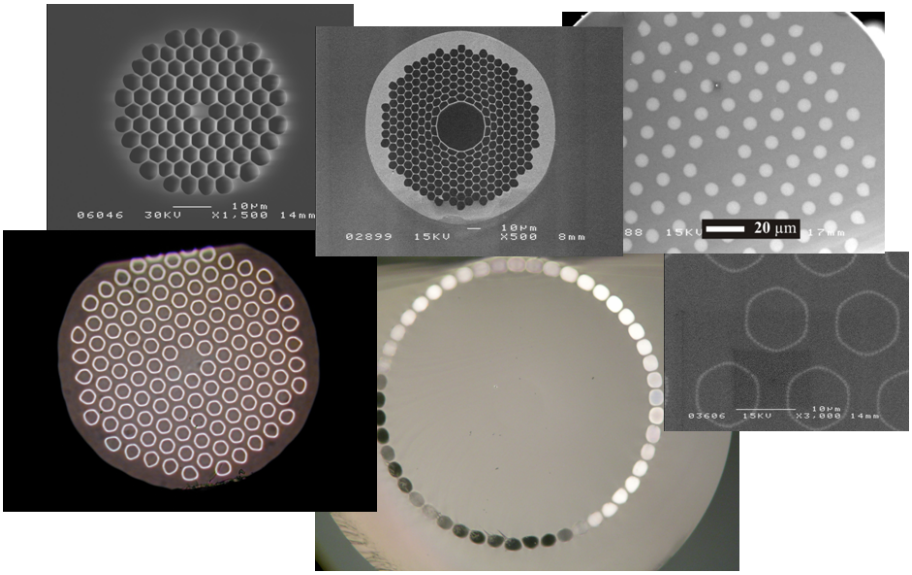

Figure 1.2: Photonic crystal fibres. Clockwise from the top left: a solid core photonic crystal fibre guiding by total internal reflection, a hollow core photonic bandgap fibre, an all-solid photonic bandgap fibre, a photonic bandgap fibre with cladding array formed of rings, an individual cane used to fabricate the ring fibre and an optical micrograph of the ring fibre.

1.2 The propagation constant

Light may only propagate in an optical fibre in one of the allowed modes, which are distributions of the electromagnetic field described mathematically by the

solutions of Maxwell's equations [17]. The number of allowed modes and the intensity distribution is governed by the physical parameters of the optical fibre [18]. The propagation constant, β, for a particular mode traveling in an optical fibre is the component of the wavevector k parallel to the core-cladding boundary and governs how the phase of the mode varies with distance. It is a useful quantity to describe propagation in optical fibres as it is conserved at boundaries parallel to the direction of propagation, i.e. the core-cladding boundary; the only non-parallel interfaces being the input and output faces of the fibre. The allowed values of β in a TIR-guiding fibre are limited by the refractive indices of the core and cladding regions and are given by

$$n_{\mathrm{cl}}k_0 \leq \beta \leq n_{\mathrm{co}}k_0 \tag{1.1}$$

where n_{cl} and n_{co} are the refractive indices of the cladding and core respectively and k_0 is the free space wavevector given by $\frac{2\pi}{\lambda}$. We can define an effective refractive index, n, of a particular mode with a propagation constant β as

$$n = \frac{\beta}{k_0}. \tag{1.2}$$

β depends on n which itself is a function of frequency, so the individual frequency components of a pulse will have different propagation constants and travel at different velocities leading to chromatic dispersion (the spreading out of the individual frequency components in the pulse envelope). Chromatic dispersion governs how the pulse width and peak intensity evolve along the fibre length, and therefore plays a critical role in most applications.

1.3 How are conventional step index optical fibres described?

Conventional optical fibres may be defined by the core-cladding refractive index contrast (Δ) and the normalised frequency known as the V parameter which governs the number of modes supported in the core for a particular wavelength of light. The parameter Δ is given by

$$\Delta = \frac{n_{\mathrm{co}} - n_{\mathrm{cl}}}{n_{\mathrm{co}}}, \tag{1.3}$$

and the V parameter is given by

$$V = k_0 a (n_{\mathrm{co}}^2 - n_{\mathrm{cl}}^2)^{\frac{1}{2}} \tag{1.4}$$

where a is the core radius, $k_0 = \frac{2\pi}{\lambda}$ and λ is the wavelength of light. In conventional optical fibres the fibre will support only the fundamental mode and no higher order modes if the condition $V < 2.405$ is satisfied [18]. If this is the case the fibre is said to be single moded. It can be seen from 1.4 that, in order for a fibre to be single moded, either a needs to be small, λ to be large or $n_{\mathrm{co}}^2 - n_{\mathrm{cl}}^2$ to be small. Commercial single mode fibres are therefore only single moded for a specific wavelength region. As a higher order mode reaches a wavelength region where it is no longer supported it is said to approach the "cut-off" wavelength.

For TIR guidance, light needs to be launched into an optical fibre so that it propagates with an angle less than the critical angle, θ_{c}. We can define an acceptance cone known as the numerical aperture (NA) as shown in fig. 1.3 for a particular fibre given by the sine of the maximum launching angle θ_{max}.

$$\sin(\theta_{\max}) = \sqrt{n_{\text{co}}^2 - n_{\text{cl}}^2}. \tag{1.5}$$

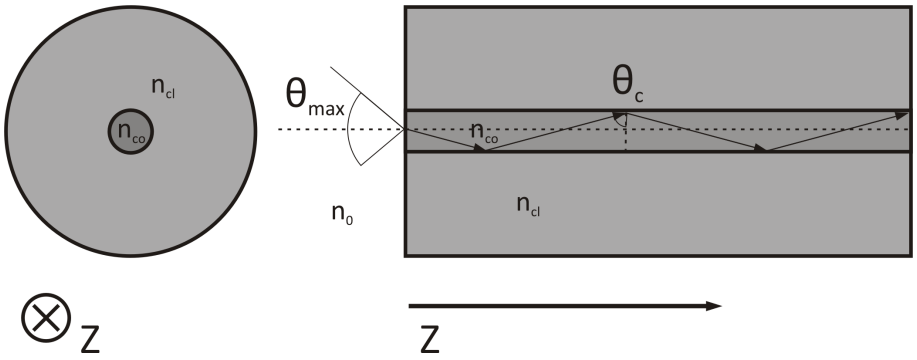

Figure 1.3: Schematic representations of the numerical aperture of a step index fibre. On the left is the fibre end face whereas the diagram on the right shows a slice along the z axis through the centre of the fibre.

For practical use of optical fibres the NA is an important quantity to know. In order to couple light from one fibre to a second fibre efficiently, lenses must be used which closely match the NAs of the fibres.

1.4 Describing photonic crystal fibres

PCFs are principally defined by three key parameters as shown in fig. 1.4: the centre to centre separation of the cladding inclusions (either air holes or doped glasses) Λ, the diameter of the cladding inclusions d, and the core diameter ρ defined as the shortest distance across the core between the closest spaced cladding inclusions.

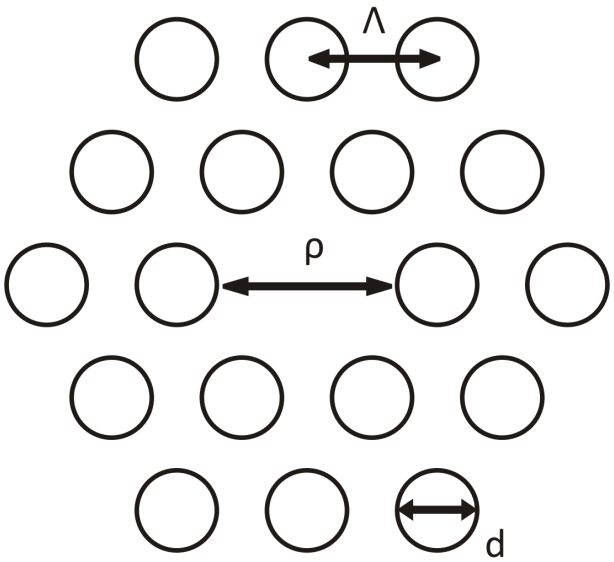

Figure 1.4: The key photonic crystal fibre parameters: Λ is the centre to centre separation of the cladding inclusions, d is the diameter of the cladding inclusions and ρ is the core diameter.

1.5 Chromatic dispersion

The effective refractive index of a confined mode in a fibre varies as a function of frequency, ω. The individual speeds experienced by different frequencies are different given by $\frac{c}{n(\omega)}$. Consider an optical pulse envelope propagating with several frequencies travelling at different speeds. The pulse envelope will spread out as it propagates, as the slower frequencies lag behind the faster ones; this process is known as chromatic dispersion. The engineering of fibre dispersion is exploited in chapters 4 and 5. In chapter 4, work is presented where a fibre is fabricated with the dispersion varying along its length in order to compress adiabatically optical pulses known as solitons. In chapter 5, work is presented where the group index (defined below) is engineered in a fibre in order to generate additional frequencies in supercontinuum generation.

To describe chromatic dispersion of a pulse propagating in an optical fibre, a Taylor expansion of β is taken around the central frequency of the pulse, ω_0, to give

$$\beta(\omega) = n(\omega)\frac{\omega}{c} = \beta_0 + \beta_1(\omega - \omega_0) + \frac{1}{2}\beta_2(\omega - \omega_0)^2 + \frac{1}{6}\beta_3(\omega - \omega_0)^3 + \dots \quad (1.6)$$

where

$$\beta_m = \left(\frac{\mathrm{d}^m\beta}{\mathrm{d}\omega^m}\right)_{\omega=\omega_0}, \qquad m = 0, 1, 2, 3, \dots \quad (1.7)$$

The coefficients β_1 and β_2 are related to the refractive index and its derivatives through the relations

$$\beta_1 = \frac{1}{v_\mathrm{g}} = \frac{n_\mathrm{g}}{c} = \frac{1}{c}\left(n + \omega\frac{\mathrm{d}n}{\mathrm{d}\omega}\right), \quad (1.8)$$

$$\beta_2 = \frac{1}{c}\left(2\frac{\mathrm{d}n}{\mathrm{d}\omega} + \omega\frac{\mathrm{d}^2n}{\mathrm{d}\omega^2}\right), \quad (1.9)$$

where v_g is the group velocity and n_g is the group index. It can easily be seen from 1.8 that the group index can be readily obtained from the second term of 1.6. Throughout this thesis we will refer to n_g and n as functions of wavelength. The parameter n_g varies as a function of n through the relation

$$n_\mathrm{g}(\lambda) = n(\lambda) - \lambda\frac{\mathrm{d}n(\lambda)}{\mathrm{d}\lambda}. \quad (1.10)$$

Both n_g and n are plotted in fig. 1.5 for bulk silica.

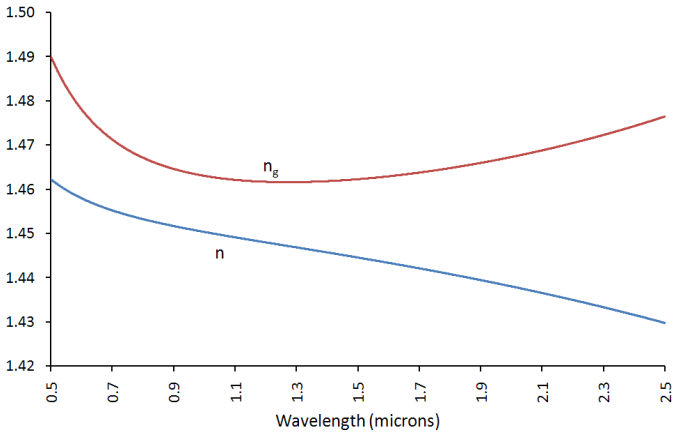

Figure 1.5: Variation of phase index and group index with wavelength for bulk silica

The coefficient β_2 determines how the individual frequencies in a pulse envelope disperse as it propagates. This is known as group velocity dispersion (GVD) and it is quantified by β_2, which is generally given in units of $\mathrm{ps}^2\ \mathrm{km}^{-1}$. Dispersion is also quantified by the dispersion parameter, D, which has arisen for practical engineering use and has units of picoseconds of spreading per nanometre of bandwidth per kilometre travelled, $\mathrm{ps\ nm}^{-1}\ \mathrm{km}^{-1}$. The parameter D is obtained from β_2 by the relation

$$D = -\frac{2\pi c}{\lambda^2}\beta_2. \tag{1.11}$$

In this thesis D will be generally used rather than β_2 and given in terms of λ rather than ω. Rewriting 1.9 for D in terms of λ we obtain

$$D(\lambda) = -\frac{\lambda}{c}\frac{\mathrm{d}^2 n(\lambda)}{\mathrm{d}\lambda^2} = c\frac{\mathrm{d}n_{\mathrm{g}}(\lambda)}{\mathrm{d}\lambda}. \tag{1.12}$$

The variation of D and β_2 with wavelength for bulk silica can be seen in fig. 1.6. There are two distinct regions, the first where D is negative (β_2 is

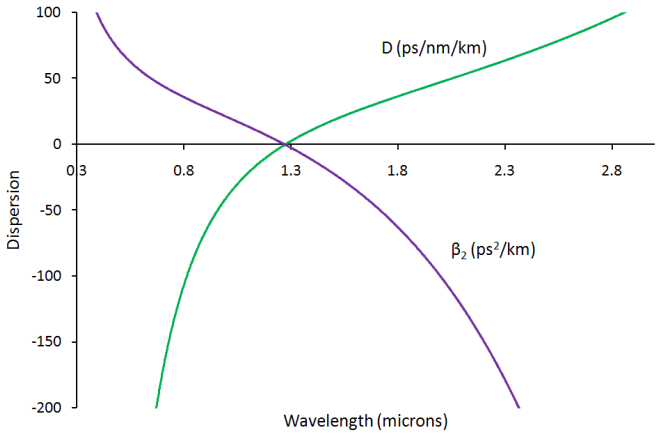

Figure 1.6: Variation of D and β_2 with wavelength for bulk silica.

positive) known as the normal dispersion regime. Here the lower frequencies travel faster than the higher frequencies, so a pulse will spread out with a frequency chirp in which the lower frequencies travel at the front of the pulse. In the second region, known as the anomalous dispersion regime, D is positive (β_2 is negative). In this region, the higher frequencies travel faster than the lower frequencies, so a pulse will spread out with the higher frequencies at the leading edge of the pulse.

1.5.1 The dispersion length

For a pulse of a given duration propagating in a fibre, we can define a characteristic length over which the effects of dispersion become important. This length is known as the dispersion length, L_{D}, and is given by the equation

$$L_{\mathrm{D}} = \frac{T_0^2}{|\beta_2|}, \tag{1.13}$$

where T_0 is the input pulse width. From 1.13 it is straightforward to note that dispersive effects become more important for shorter pulses. The physical ex-

planation for this is that a shorter transform limited pulse will have broader bandwidth than a pulse of longer temporal duration, and will therefore experience a greater degree of spreading.

1.5.2 Dispersion engineering

This section describes how the cladding of index guiding PCFs can engineered and the subsequent effect on the dispersion of the fibre. The ability to engineer the dispersion, a linear property, of PCFs underpins the nonlinear work presented in chapters 4 and 5.

There are two contributions to the overall dispersion of an optical fibre: material dispersion and waveguide dispersion. Material dispersion is the intrinsic dispersion of a bulk medium arising from the interaction between an electromagnetic wave and the electrons in the medium. The proximity in wavelength of the electromagnetic wave to the electronic resonances of the medium affect the response of the medium. It is this which accounts for the wavelength dependence of the refractive index in bulk media. As well as the contribution to the dispersion from the bulk material, there is also a waveguide contribution to the dispersion arising from the confinement of optical waves. For conventional optical fibres (which have a core-cladding index contrast of only 1-2%) there is only a slight modification from the bulk silica dispersion curve, although introducing rings of different dopants around the core and tapering the fibre can be used to adjust the slope and position of the zero dispersion wavelength [19, 20]. As PCFs have a large core-cladding index contrast, the contribution from the waveguide dispersion can be quite large, significantly altering the overall dispersion from that of the bulk material.

To understand why the waveguide contribution to the dispersion can be so large in PCFs it is useful to look back to the phase index n. Fig. 1.7a shows n as a function of wavelength for bulk silica, and also the fundamental modes

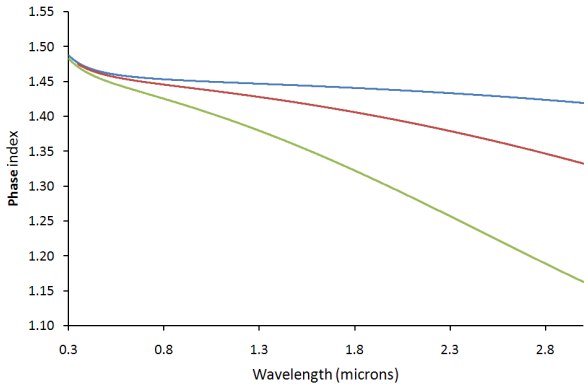

(a)

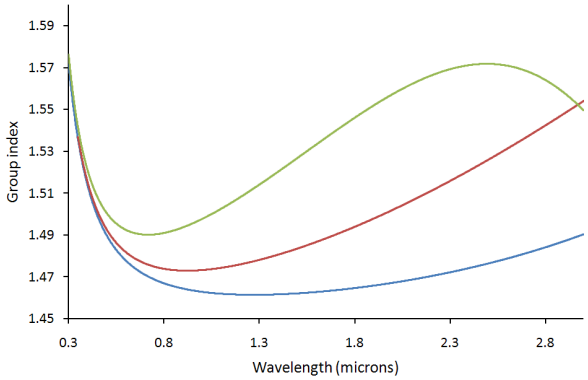

(b)

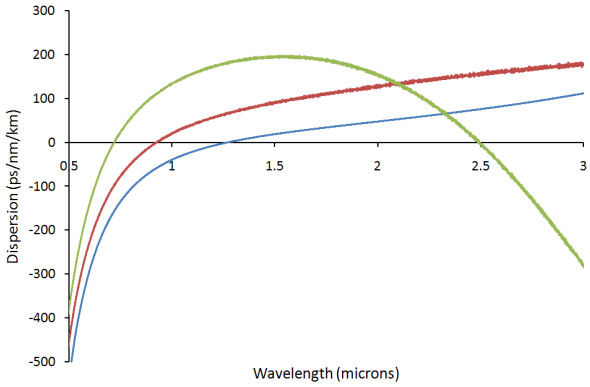

(c)

Figure 1.7: The variation of n, n_g and D with wavelength for bulk silica (blue), a 4 μm silica strand surrounded by air (red), and a 2 μm silica strand surrounded by air (green).

of a 4 μm diameter silica strand and a 2 μm silica strand both surrounded by air. These are good approximations to high-Δ PCFs. For λ <400 μm there is little difference between the strands and the bulk material. This is because the the wavelength here is small, and therefore most of the light is guided in the strand and does not spread far into the air "cladding". The result is that there is little deviation from the phase index of the bulk material. As λ increases a mode in a strand will become larger and more light will propagate outside the the strand in the air; this is accentuated for smaller strands. As a result, the deviation from the bulk material becomes larger as the phase indices of the strands tend towards that of air ($n = 1$). 1.10 gives the relationship between the group index and the phase index. The last term on the right-hand side depends on $\frac{\mathrm{d}n}{\mathrm{d}\lambda}$. In the case of silica this is negative, making the overall contribution to the group index of the last term positive. The size of the contribution depends on the magnitude of the slope, which, at shorter wavelengths, is larger for smaller cores. As the phase index approaches 1 the magnitude of the slope becomes smaller and provides a second inflection point. The inflection points in the phase index provide the maxima and minima in the corresponding group index curves, fig. 1.7b. We can extend this to see how the GVD is varied through 1.12 which is proportional to $\frac{\mathrm{d}n_\mathrm{g}(\lambda)}{\mathrm{d}\lambda}$. The maxima and minima in the group index curves give rise to points of zero GVD as shown in fig. 1.7c. Regions where $\frac{\mathrm{d}n_\mathrm{g}(\lambda)}{\mathrm{d}\lambda}$ is large give large dispersion.

The effective refractive index of PCF cladding structures can be approximately varied anywhere between that of silica and that of air by changing the size and separation of the air holes. A plane wave travelling in an infinite PCF cladding array will propagate with a propagation constant defined by the fundamental space filling mode (FSM) β_fsm [6]. The effective refractive index of the cladding can be defined by

$$n_\mathrm{fsm} = \frac{\beta_\mathrm{fsm}}{k_0}. \tag{1.14}$$

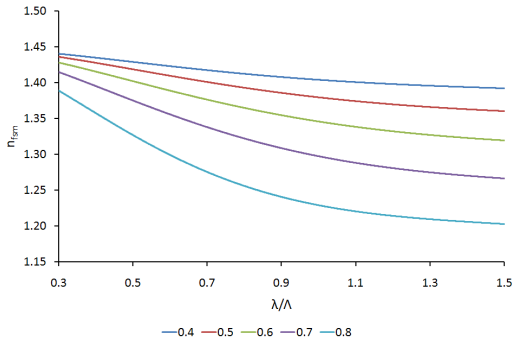

Figure 1.8: The effective refractive index of the fundamental space filling mode against normalised wavelength for five infinite PCF cladding arrays. d/Λ =0.4, 0.5, 0.6, 0.7 and 0.8 for blue, red, green, purple and cyan respectively.

Fig. 1.8 shows the effective refractive indices of infinite cladding arrays with different d/Λ ratios against normalised wavelength. When the wavelength becomes as large as Λ, the effective index can be seen to tend towards different values between the refractive indices of n_{air} and n_{silica}.

The effect of different cladding structures on different fibre properties is shown in fig. 1.9. Here n, n_{g} and D are plotted against wavelength for five different cladding d/Λ ratios all with a pitch of $2\,\mu$m. The different d/Λ ratios give different effective indices for the claddings, so the phase indices tend to different values of n lying between n_{air} and n_{silica}. As the core-cladding index contrast decreases (d/Λ decreases), the confinement of the mode to the core region becomes weaker, allowing the mode to spread further into the cladding with increasing wavelength. This can be seen by comparing fig. 1.9a and fig. 1.8. The effective index in a small d/Λ PCF tends towards the effective cladding index at shorter wavelengths than for larger d/Λ ratios. Careful selection of the core size and cladding parameters allow fibres with tailored dispersion profiles to be produced. Some notable reported PCFs with tailored dispersion profiles include: ultra flattened (Reeves et al. [21] demonstrated a PCF with a flat dispersion profile, to reduce higher order dispersion, close to zero between 1.1 to 1.6 μm), multiple zero, zero dispersion shifted [22] and even tapered by adjusting the air holes along the length of the fibre [23].

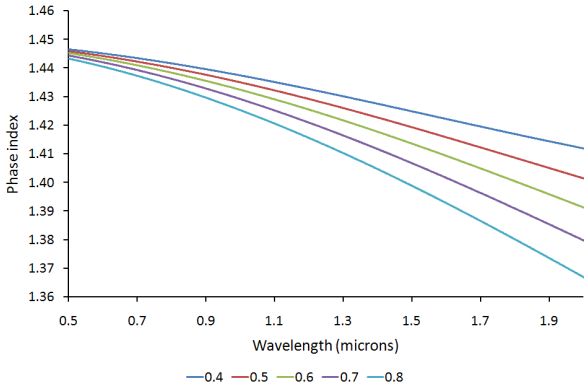

(a)

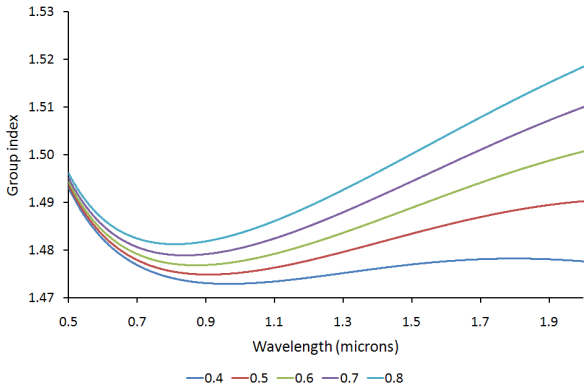

(b)

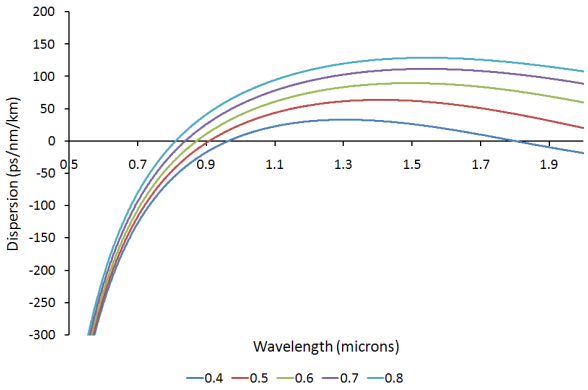

(c)

Figure 1.9: Phase index, group index and dispersion plotted as a function of wavelength for fibres where d/Λ =0.4, 0.5, 0.6, 0.7 and 0.8. In each case Λ=2.0 μm.

1.6 Loss

No optical fibre guides light without some degree of power loss as the light propagates. Loss is generally expressed in optical fibres on a logarithmic scale with units of dB/km. The loss α is given by

$$\alpha = -\frac{10}{L}\log\left(\frac{P_{\text{out}}}{P_{\text{in}}}\right) \tag{1.15}$$

where L is the distance along the fibre and $\frac{P_{\text{out}}}{P_{\text{in}}}$ is the ratio of output power to input power. In silica optical fibres there are several contributions to the overall loss, shown in fig. 1.10. The window over which silica is transparent spans from approximately 0.2 to 2.5 μm. The ultraviolet edge is limited by electronic absorption and the infrared edge is limited by the absorption of the silica bonds. The fundamental loss below 1.55 μm is not due to the electronic absorption, but instead due to Rayleigh scattering which scales with λ^{-4}. Rayleigh scattering governs the fundamental limit for the lowest loss as it arises from density fluctuations frozen into the fibre during fabrication [24]. Curves of loss vs wavelength for multimode fibres fabricated from Heraeus Fluosil preforms [25] are shown in fig. 1.10. The cladding regions are all fluorine doped silica and the core regions are formed from different grades of silica. In addition to these intrinsic losses, silica fibres are also very sensitive to impurities. In particular OH^- ions have a strong absorption close to 2.7 μm, and several overtones are particularly prominent [26] as seen in fig. 1.10 as peaks at 1.4 μm and 1.2 μm. These peaks arise through contamination from water molecules, so every effort to keep the silica "dry" throughout the fibre fabrication process must be made. The reduction of OH^- ions during the glass fabrication process can be done with the introduction of Cl^- ions; however, this introduces chlorine absorption bands in the ultraviolet region of the spectrum.

Initial predictions for hollow-core PCFs implied that it may be possible to

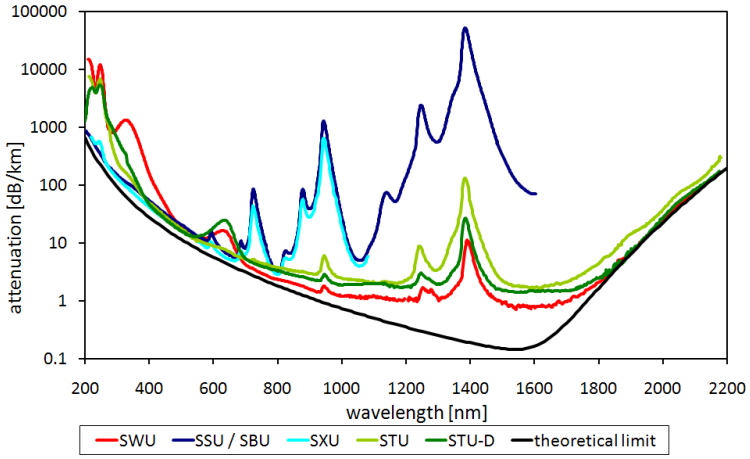

Figure 1.10: Loss curves for multimode fibres with different core glasses available from Heraeus. SWU has an F300 core, the lowest water content pure fused silica available from Heraeus with less than <0.7 ppm OH^-. This low figure is achieved using chlorine in the fabrication process which has its own absorption peaks visible in the ultraviolet region. SSU/SBU and SXU are formed from pure silica which has not been treated with chlorine (F100 and F110). This achieves better transmission than F300 in the ultraviolet region but has significantly larger OH^- content. STU and STU-D are fluorine doped (F320) with OH^- contents of 1-20 ppm and <1 ppm respectively. All the cladding regions are formed from fluorine doped silica.

obtain lower losses than low-loss conventional long-haul telecommunications fibres ($\approx$ 0.2 dB/km). This is because light is propagating in air with only a small overlap with a silica core wall, which will virtually eliminate all the above loss mechanisms. However, Roberts et al. [27, 28] reported that air-silica microstructured fibres suffer from their own loss mechanism. Roughness at air-silica interfaces couples light out of the guided core mode and into lossy cladding modes. This limits the best hollow core fibre losses to just above that of conventional low-loss fibres at $\approx$ 1.2 dB/km.

Solid core PCFs, in general, are used for nonlinear applications; this is the case in the work detailed in the latter chapters of this thesis. The enhanced confinement of light to the core and the ability to engineer the dispersion leads to nonlinear effects occuring over far shorter distances than in conventional

optical fibres. This places less of an importance on the loss of these fibres, however, loss still plays its part in many cases. In supercontinuum generation light can be generated in the blue and ultraviolet regions as well as >2100 nm where the loss is in excess of 100 dB/km, this will eventually limit the generated continuum. Typical fibre lengths for continuum generation therefore range from 2 m for femtosecond pulses to 10 m for sub-nanosecond pulses.

In addition to these intrinsic losses, optical fibres can also suffer losses when the fibre is bent. In chapter 3 a method for fabricating all solid bandgap fibres with reduced bend losses is presented. Bend loss in conventional optical fibres and all-solid bandgap fibres is discussed in detail in chapter 3.

1.7 Bandgap guidance in all solid photonic bandgap fibres: the ARROW model

The most universally accepted model for bandgap guidance in PCFs is known as the anti-resonant reflecting optical waveguide or ARROW model. The ARROW model was first proposed as an explanation for bandgap guidance in PCFs by Litchinitser et al. [29, 30], although a similar theory for one-dimensional periodically planar waveguides, where light is confined by a series of high and low index regions, had long been in existence [31, 32]; fig. 1.11a. This 1d model provides an easy way to understand the physical concept, so it will be discussed first and then extended to PCFs. The fibres we will consider consist of a two dimensional array of high index circular rods embedded in a low index background, with a single rod missing forming a low index defect region in which light can be confined. A similar structure is used in all-solid photonic bandgap fibres [15, 16, 33], see fig. 1.11b.

The ARROW model is based around a consideration of the individual modes of the high index regions. The high index regions in the case of all-solid

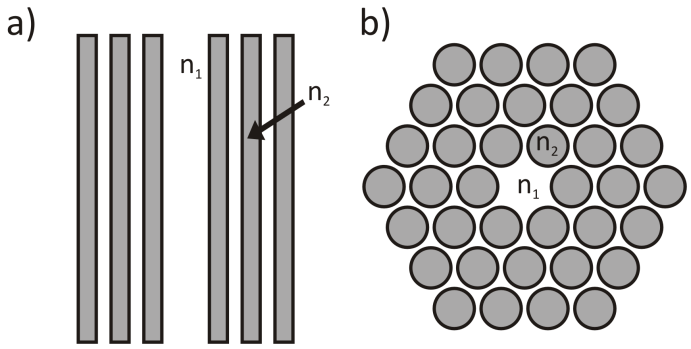

Figure 1.11: Schematic diagrams of a) a one dimensional anti-resonant planar waveguide (the core is running vertically) and b) an all-solid photonic bandgap fibre with the core defect running into the page. In both cases high index regions, n_2, are darker grey and the low index background material, n_1, is white. The low index core defects in which the light is confined by anti-resonant reflection are formed in both cases by the omission of one high index region in an otherwise regular array.

photonic bandgap fibres can be considered as an array of conventional step index fibre cores and in the planar waveguide are considered to be a series of Fabry-Perot resonators [34]. In the one dimensional case, when the wavelength of light in the core matches a resonant wavelength of the Fabry-Perot, cavity the light will be transmitted out of the core through the high index resonator; see fig. 1.12a. Away from this resonant wavelength the light will be reflected back and confined to the core of the waveguide, as shown in fig. 1.12b.

The anti-resonant case is when the wavelength of the light inside the cavity is half-way between two consecutive cavity resonances, although light will be reflected back for any wavelength away from a cavity resonance (fig. 1.12b). Extending this to the 2d array of high index cores, the resonant modes of the cavity are analogous to the modes of the high index cores at their cutoff wavelengths. The cutoff wavelength for a particular mode is the longest wavelength for which the mode can still be supported in a high index core, i.e. above this wavelength the core can support m modes and below it can support $m + 1$ modes. When light is incident on a high index core at a cutoff wavelength, it will be resonantly coupled out of the low index core defect. This manifests it-

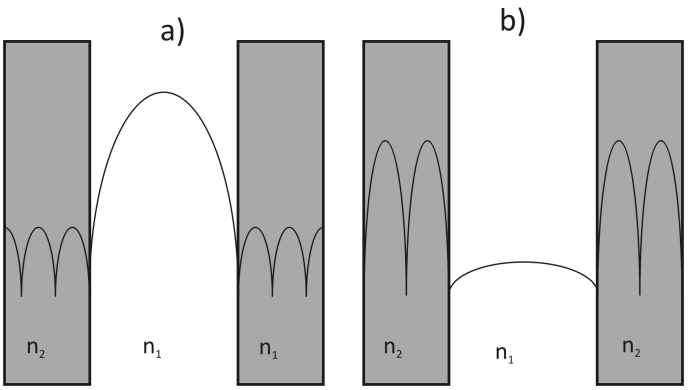

Figure 1.12: Schematic representations of the intensity profile in the core region and first high index regions in the one dimensional planar waveguide, a) is the anti-resonant case where light is confined in the core region by anti-resonant reflections and b) is when the wavelength is close to a resonance of the high index regions corresponding to the peak transmission of the Fabry-Perot cavity.

self as sharp high loss regions in the transmission spectrum of the fibre. Again, away from the resonant wavelengths the light is reflected back and confined in the low index core. In the ARROW model, the locations of the band gap edges are independent of the separation and location of the high index regions, depending only on the size, shape and refractive index (i.e. the quantities which affect the modes) [16, 29, 30, 35, 36] of the high index resonators.

1.8 Fabrication

Fabrication of both PCF and conventional optical fibre requires first the creation of a macroscopic preform of the desired microscopic fibre structure. These preforms are then drawn to fibre on a fibre drawing tower in a similar manner to the fabrication of seaside rock [37]. There are a number of ways of fabricating PCF preforms, with the most common being the stack and draw method (fig. 1.13). First, capillaries are drawn from glass tubes and then stacked in a close packed array with any solid defects (such as the core)

created by the replacement of a capillary with a solid rod. This "stack" is then inserted into a tube (typically 20-25 mm in diameter), and put on a fibre drawing tower, and drawn down to the preforms (typically 1-4 mm in diameter). These preforms provide a useful intermediate stage before drawing to fibre. The holes in the preforms are generally pressurised as they are drawn to fibre. This can maintain the structure, or allow the holes to collapse or to be inflated. It is even possible to apply different pressures to different holes by inserting capillaries into them and pressurising the capillaries; this technique has been used to make polarisation-maintaining PCFs [38].

PCF preforms can also be created by drilling the desired structure into a solid rod. This technique not only limits the length of the preforms by the length of the drill bit, but also requires the silica cladding web to be thick walled in order to prevent the walls from breaking.

PCFs fabricated from soft glasses such as tellurite have also been reported [39–41]. Here, the lower melting point of the glass allows preforms to be fabricated by extruding pellets of the glass through a metal die.

1.9 Summary

This chapter has given an introduction to the linear properties of PCFs. The ARROW model, discussed in section 1.7, describes the the guidance mechanism of AS-PBGFs. The linear guidance properties of AS-PBGFs are explored in chapter 3, where the shape of the high-index inclusions in the cladding are changed in order to change the modal properties of the cladding. The ability to engineer the dispersion of PCFs by modifying the cladding (section 1.5.2) is of particular relevance to chapters 4 and 5. The work in chapters 4 and 5, however, lies in the field of nonlinear optics, which will be discussed in the following chapter.

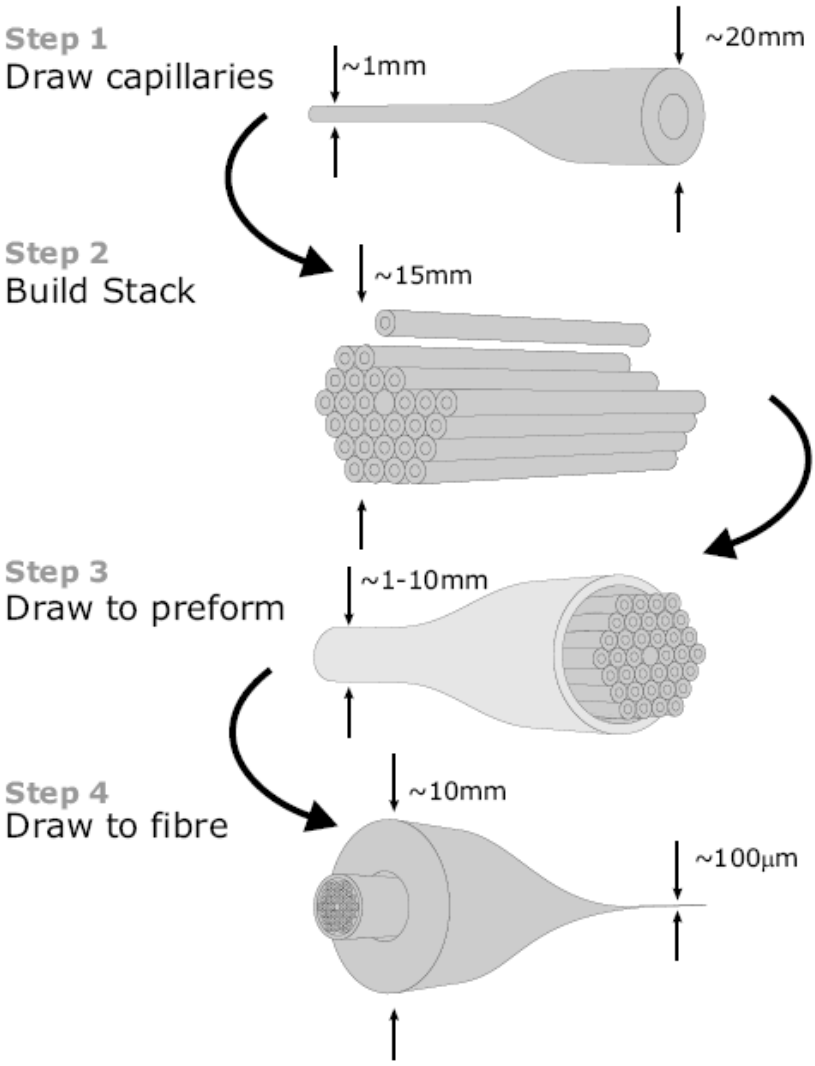

Figure 1.13: A schematic representation of the stack and draw method of PCF fabrication. First, capillaries are drawn from pure silica tubes (1) and are then stacked in a close packed array with the introduction of a defect region to form the core (2). These are drawn down to preforms (3) which are then jacketed in a silica tube and drawn to fibre (4).

Chapter 2

Nonlinear optics

2.1 Introduction

This chapter moves on from linear properties of optical fibres and describes nonlinear optical effects which are key for understanding chapters 4 and 5. As with chapter 1 it is not intended to give a comprehensive understanding of optical nonlinearity (there are significantly sized textbooks available [42, 43]), but should be viewed as a reference point for chapters 4 and 5. First we will explore the fundamental reasons for optical nonlinearity and then we will discuss nonlinear effects of specific importance to the latter chapters of this thesis.

2.2 The origins of optical nonlinearities

The response of any dielectric to an incoming electromagnetic wave is determined by the response of the outer, loosely bound, valence electrons. The

incoming wave gives rise to a polarisation p, whose scalar form is given by $p = \epsilon_0 \chi E$, where E is the electric field of the incoming wave, χ is the susceptibility of the material and ϵ_0 is the permittivity of a vacuum. Under intense fields, the response of the electrons becomes nonlinear. To describe mathematically this χ, is replaced with a Taylor expansion to give the polynomial approximation

$$p = \epsilon_0 \sum_n \chi_n E^n, \tag{2.1}$$

where χ_1 is the first order linear contribution to the susceptibility. The lowest order nonlinear term that is important for optical fibres is χ_3. The even terms are only non-zero for materials which do not possess inversion symmetry, i.e. in which the energy required to drive the electrons up is not equal to the energy required to drive them down. In such a material, in 1d, the potential energy, V, is described as a function of displacement, x, by $V(x) \neq V(-x)$. Crystals in which $\chi_2 \neq 0$ are responsible for effects such as frequency doubling [18]. χ_3 gives rise to three principal nonlinear effects: the Kerr effect, and two stimulated inelastic scattering processes: stimulated Raman scattering (SRS) and stimulated Brillouin scattering (SBS).

2.2.1 The Kerr effect

The optical Kerr effect gives rise to an intensity-dependent refractive index change, Δn, and from this most known nonlinear effects arise. The total refractive index of a material can be written as

$$n_{\text{tot}} = n + \Delta n = n + n_2 I, \tag{2.2}$$

where n is the linear refractive index, n_2 is a constant for a given material known as the nonlinear index coefficient, and I is the intensity of the incoming light. In general, n_2 is small ($3 \times 10^{-23}\,\mathrm{m^2W^{-1}}$ in air and $2 \times 10^{-20}\,\mathrm{m^2W^{-1}}$ in silica) so its effects are negligible unless the intensity is high or the interaction lengths are long. It is this that gives silica optical fibres a distinct advantage as a medium to observe nonlinear effects; optical pulses can be propagated over kilometres with losses of a fraction of a dB [44]. Nonlinear refraction is the root of effects such as self phase modulation (SPM) (and optical solitons), four-wave mixing (FWM), modulation instability (MI) and cross phase modulation (XPM). These will be discussed in detail later in this chapter.

As n_2 is generally small, the induced index change is only seen for high intensities. A result of this is it is difficult (but not impossible [45]) to observe nonlinear effects from lasers in the continuous wave (CW) regime, where the powers typically range from a few milliwatts to a few tens of watts. Instead, pulsed lasers are used where the peak powers of the pulses are several orders of magnitude higher.

2.2.2 Stimulated inelastic scattering processes

SRS and SBS both cause a transfer of energy from an electromagnetic wave to the dielectric medium in which it is propagating, producing photons down-shifted in frequency [42]. In the case of SBS, energy is transferred to an acoustic phonon and a frequency down shifted optical photon propagating in the opposite direction to that of the incident photon. It is also possible to use SBS to gain frequency up-shifted photons given an available phonon of the correct energy and momentum. In SRS, energy is transferred from the incident wave to the vibrational and rotational modes of the molecules in the dielectric, with the resulting down-shifted photons propagating in the same direction as the incident photons. It is possible for two co-propagating laser beams of different frequency to transfer energy between each other via SRS, with the

lower frequency beam gaining energy at the expense of the higher frequency beam. This effect has found uses in Raman lasers and Raman amplifiers [46]. In the case of ultrashort (<0.5 ps) pulses with large bandwidths, the higher frequencies within the pulse can act as a pump for the lower frequencies which constantly shifts the pulse to longer wavelengths [47, 48]. This is known as *intrapulse* Raman scattering and is a very useful effect for the generation of new optical frequencies. Specific Raman peaks have also been generated in gas filled hollow core photonic crystal fibres and used to generate frequency combs spanning multiple octaves [49, 50].

2.3 Quantifying nonlinearity in optical fibres

Nonlinearity in waveguides is quantified in terms of a nonlinear parameter known as γ, which takes the form

$$\gamma = \frac{n_2 \omega_0}{c A_{\text{eff}}}, \tag{2.3}$$

where A_{eff} is the effective area of the guided mode. For a normal mode electric field distribution of $E(x, y)$ A_{eff} is given by the integral

$$A_{\text{eff}} = \frac{\left(\iint_{-\infty}^{\infty} |E(x,y)|^2 \, \mathrm{d}x\mathrm{d}y \right)^2}{\iint_{-\infty}^{\infty} |E(x,y)|^4 \, \mathrm{d}x\mathrm{d}y}. \tag{2.4}$$

In practice, for optical fibres, this depends on the fibre parameters such as the physical core size and core-cladding refractive index difference. As A_{eff} is small in optical fibres, γ can be large.

Analogous to the dispersion length defined in 1.5.1, we can define a nonlinear length, the characteristic length scale over which nonlinear effects become important

$$L_{\mathrm{nl}} = \frac{1}{\gamma P_0}, \tag{2.5}$$

where P_0 is the peak power of the input pulse. It is clear from 2.5 that a large γ (or long interaction lengths) essential for efficient nonlinear observations. As the value of n_2 for a given material is fixed, the only way of increasing γ at a fixed ω in optical fibres is to reduce the effective core area. Large index contrasts, which lead to tighter confinement, give PCF withn a high air filling fraction a higher γ. An in-depth discussion of the nonlinear characterisation of different kinds of optical fibres can be found in chapter 11 of the fourth edition of ref. 42.

2.4 Self phase modulation

Self phase modulation (SPM) occurs when a pulse acts on itself through the instantaneous change in refractive index $n_2 I$. It refers to a self-induced shift in the phase of the pulse, which is proportional to the rate of change of intensity with time, $\frac{\mathrm{d}I}{\mathrm{d}t}$, as the pulse propagates along the fibre length. When the index change from one pulse acts on a second pulse to induce a phase shift the effect is known as cross phase modulation (XPM). As a result of SPM, ignoring dispersive effects, a spectral chirp will be induced across the pulse as it travels, with no change to the temporal width of the pulse. As the chirp depends on $\frac{\mathrm{d}I}{\mathrm{d}t}$, it will always be positive for a positive n_2. The leading edge of the pulse, where $\frac{\mathrm{d}I}{\mathrm{d}t}$ is positive, will generate new red-shifted frequencies, and the trailing edge, where $\frac{\mathrm{d}I}{\mathrm{d}t}$ is negative, will generate new blue-shifted frequencies. The relationship to $\frac{\mathrm{d}I}{\mathrm{d}t}$ results in the effects of SPM becoming stronger for shorter

pulses.

Practically, however, dispersive effects can rarely be ignored in optical fibres. The effects of different dispersive regimes when combined with the effects of SPM lead to very different results. In the normal dispersion regime, a pulse undergoes temporal lengthening as the lower frequencies travel with a higher group velocity than the higher frequencies. This leads to a positive spectral chirp. When combined with SPM, this dispersion of the pulse is enhanced by the new frequencies generated but, as the pulse propagates and spreads, the peak intensity is reduced. This reduces $\frac{\mathrm{d}I}{\mathrm{d}t}$ and hence the effects of SPM. In the anomalous dispersion regime, where a pulse acquires a negative chirp as it spreads out in time, the effects of SPM can counter this spreading to form stable pulses known as solitons, which can propagate unperturbed [18, 42, 51, 52].

2.5 The nonlinear Schrödinger equation

The dynamics of pulse propagation in optical fibres are described by the nonlinear Schrödinger equation (NLSE), the derivation of which can be found in many textbooks and publications [42, 51, 53]. When describing it here, we will notate it using the dimensionless terms defined by

$$\tau = (t - \frac{Z}{v_\mathrm{g}})/T_0, \qquad z = Z/L_\mathrm{D}, \qquad u = \sqrt{|\gamma|\, L_\mathrm{D} A}, \tag{2.6}$$

where t is time, Z is propagation distance, T_0 is a temporal scaling parameter often taken to be the input pulse duration, and A is the pulse amplitude. Including terms which govern higher order effects, the NLSE then takes the form

$$i\frac{\partial u}{\partial z} \pm \frac{1}{2}\frac{\partial^2 u}{\partial \tau^2} + |u|^2 u = i\delta_3 \frac{\partial^3 u}{\partial \tau^3} - is\frac{\partial}{\partial \tau}(|u|^2 u) + \tau_{\mathrm{r}} u \frac{\partial |u|^2}{\partial \tau}. \tag{2.7}$$

In this equation the second term on the left-hand side describes the effects of second order dispersion and is positive for pulse propagation in the anomalous dispersion regime; the third term describes the effects of nonlinearity. The higher order terms are collected on the right-hand side. The first term on the right describes the effects of third order dispersion where $\delta_3 = \frac{\beta_3}{6|\beta_2|T_0}$. The second term on the right describes the effects of self steepening where $s = \frac{1}{\omega_0 T_0}$. In the absence of dispersion and other higher order effects, this shock term leads to the formation of a shock front at the trailing edge of the pulse. This is due to the intensity dependence of the group velocity, causing the centre of the pulse to travel slower than either edge. The final term on the right describes the effects of intrapulse Raman scattering, where $\tau_{\mathrm{r}} = \frac{T_{\mathrm{r}}}{T_0}$ and T_{r} is the Raman time constant which is related to the slope of the Raman gain for a given frequency [54].

When pulses in silica optical fibres are greater in duration than $\approx 1\,\mathrm{ps}$, the bandwidth of the pulse becomes sufficiently small for several approximations to be made in deriving the NLSE [42]. This pulse duration corresponds to a bandwith of $\approx$0.1 THz, sufficient the Raman gain (the most dominant higher order effect) to amplify the lower frequencies of the pulse at the expense of the higher frequencies continually shifting it to shorter wavelengths. Neglecting higher order terms 2.7 is simplified to

$$i\frac{\partial u}{\partial z} + \frac{1}{2}\frac{\partial^2 u}{\partial \tau^2} + |u|^2 u = 0. \tag{2.8}$$

In practice the NLSE is difficult to solve analytically, and a numerical approach is needed. The most commonly used method is the split step Fourier method in which the dispersive and nonlinear parts of 2.7 are split up and solved in turn for small propagation steps [55, 56].

2.6 Solitons

This section describes the dynamics of fundamental and higher order solitons, both of these are used to describe the results in chapters 4 and 5.

Optical solitons are pulses formed when the effects of nonlinearity and dispersion are made to balance one another. Soliton propagation can be easily understood as a two step process if we separate the effects of dispersion and nonlinearity. Anomalous dispersion (fig. 2.1b), like normal dispersion, lengthens an initially transform-limited pulse in a fibre. In the case of an initial positive chirp, anomalous dispersion will act to rectify the chirp and compress the pulse. SPM imposes such a chirp on a pulse without temporally spreading the pulse. Consider first SPM acting on a pulse alone with $\beta_2 = 0$. The pulse will acquire a positive chirp (fig. 2.1c) with the generation of new frequencies. If we then switch off SPM and set $\beta_2 < 0$, the dispersion will compensate for the chirp. This process could be repeated to propagate pulses in such a way that the two effects continually counteract each other. In practice, both of these effects occur simultaneously to form pulses which propagate undistorted.

In order to describe soliton dynamics, we define the dimensionless parameter N in terms of two input pulse parameters T_0 and P_0 and the two waveguide parameters γ and β_2:

$$N^2 = L_{\mathrm{D}}\gamma P_0 = \frac{\gamma P_0 T_0^2}{|\beta_2|}. \tag{2.9}$$

IF $N = 1$, the soliton takes the form of the pulse described above and propagates without temporal or spectral distortion. This is known as the fundamental soliton and has the form

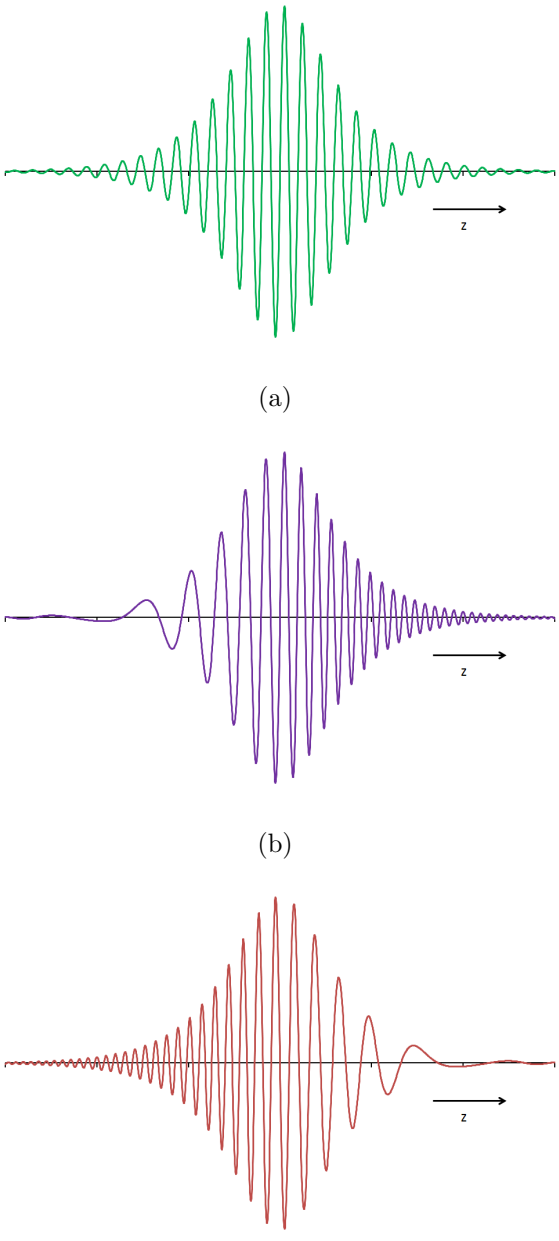

(a)

(b)

(c)

Figure 2.1: Schematic representations of frequency chirp induced on an initially unchirped pulse (a). (b) shows pulse travelling with anomalous group velocity dispersion and (c) shows the chirp for a pulse travelling with self phase modulation.

$$u(z,\tau) = \operatorname{sech}(\tau)\exp\left(i\frac{z}{2}\right), \tag{2.10}$$

which is a solution to 2.8. If, however, N has an integer value such that $N > 1$, the pulse propagates as a higher order soliton. The soliton evolves periodically both spectrally and temporally, returning to its original shape over a characteristic length known as the soliton length, z_0, given by

$$z_0 = \frac{\pi}{2}L_{\mathrm{D}} = \frac{\pi T_0^2}{2\left|\beta_2\right|}. \tag{2.11}$$

The quantities N and z_0 play a vital role in describing soliton dynamics. The evolution of a higher order soliton ($N = 3$) over two soliton periods is shown in fig. 2.2; the initial input pulse had a duration of 50 fs and a central wavelength of 800 nm.

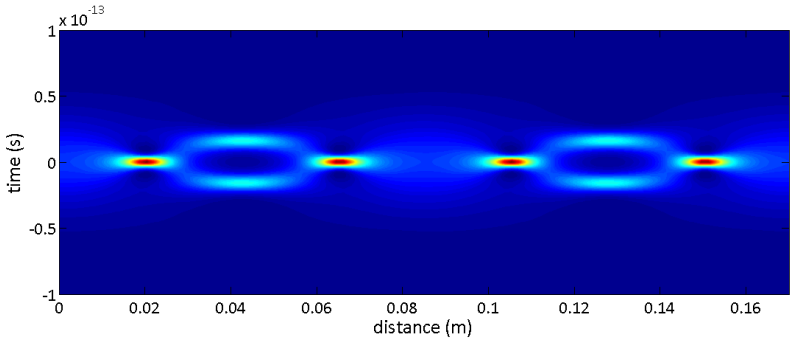

Figure 2.2: Temporal evolution an $N = 3$ soliton over two soliton periods. The intensity colour map is shown on a linear scale.

2.6.1 Intrapulse Raman scattering and soliton fission

The inclusion of the Raman term in 2.7 significantly alters the dynamics of soliton propagation for ultrashort pulses. In the ultrashort regime, the bandwidth of the fundamental soliton is sufficiently large for the higher frequencies

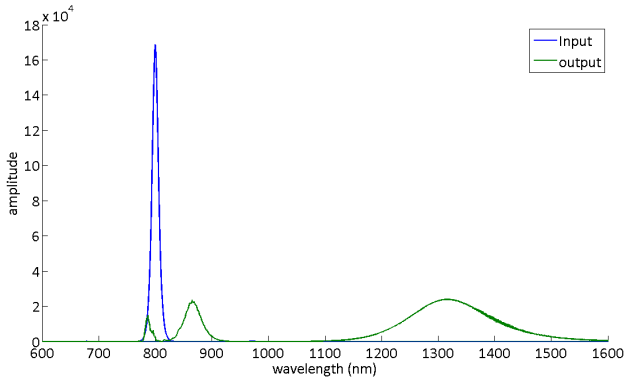

Figure 2.3: Modelled spectral input (blue) and output (green) of an $N = 3$ soliton after propagating 4.7 soliton periods with the inclusion of the Raman contribution.

in the pulse to pump the lower frequencies, leading to a continuous down-shift of the central frequency of the pulse. For higher order solitons, the effect causes the pulse to be split up with the energy being ejected from the pulse as several fundamental solitons. This process is known as soliton fission, and it occurs as the effects of Raman scattering perturb the propagation of higher order solitons. The perturbation effects of higher order dispersion can also lead to soliton fission; however, the Raman effect in most cases is generally stronger and dominates [57]. As stated earlier, higher order solitons undergo spectral and temporal oscillations as they propagate. At the point of maximum temporal compression, the duration of the solitons can be very short, leading to a very broad bandwidth; it is at this point that soliton fission generally occurs. A soliton of order N will split up into N fundamental solitons which are ejected from the pulse in turn. The solitons are ejected in order of peak power, with the highest power (temporally shortest) being ejected first. The ejected solitons then shift to longer wavelengths through intrapulse Raman scattering. Fig. 2.3 shows the spectral effects of including the Raman term on an $N = 3$ soliton, after ≈ 4.7 soliton periods. The input parameters are the same as shown in fig. 2.2b; three fundamental solitons can be seen to have been ejected which have shifted to longer wavelengths via intrapulse Raman scattering.

2.6.2 Dispersive wave generation

The effect of higher order dispersion on solitons leads to the generation of a packet of higher frequency dispersive radiation and has been expressed as an optical manifestation of Cherenkov radiation [58]. The radiation is coupled to a narrow band resonance in the normal dispersion regime such that the condition $\beta_{\mathrm{d}}(\omega_{\mathrm{d}}) = \beta_{\mathrm{s}}(\omega_{\mathrm{s}})$ is satisfied, where β_{d} and β_{s} are the propagation constants as functions of the frequencies ω_{d} and ω_{s} for the generated radiation and soliton respectively [59, 60]. This is a narrow band resonance and has to lie within the bandwidth of the soliton, so generally only occurs when the soliton is propagating close to the zero dispersion wavelength. In the case of higher order solitons, the large spectral broadening experienced in the soliton cycle can allow the soliton to be propagating further from the zero dispersion wavelength and still overlap with the resonance [57].

2.7 Four-wave mixing

Four-wave mixing is an important nonlinear mechanism in terms of new frequency generation, as it allows the generation of new frequencies in spectral regions relatively far from the pump. The mechanism again relies on the induced refractive index change from the χ_3 susceptibility. Two photons of frequencies ω_1 and ω_2 annihilate one another to form two more photons: one shifted up in frequency (signal, ω_3) and one shifted down (idler, ω_4) in order to conserve energy:

$$\omega_1 + \omega_2 = \omega_3 + \omega_4. \tag{2.12}$$

FWM is a parametric process (the medium in which the event occurs plays a passive role, unlike stimulated inelastic processes), so in order for it to occur

the phase matching condition must be satisfied such that the the sum of the wavevectors (Δk) is conserved:

$$\Delta k = \beta_3 + \beta_4 - \beta_1 - \beta_2 = 0, \tag{2.13}$$

where β_i refer to the propagation constants for the individual waves involved [42]. This condition is automatically satisfied for the degenerate case ($\omega_1 = \omega_2$) if the pump providing the two incident photons is close to the zero dispersion wavelength of the fibre. The new frequencies generated from FWM require a seed from which to grow, which can either be background noise or a separate weak seed pump source simultaneously launched into the fibre.

2.8 Supercontinuum generation

Supercontinuum generation is the generation of a wide spectrum of frequencies from a narrow band pump. Essentially a white light source can be produced that has the brightness of a laser. It is not one nonlinear process in itself, but a multitude of nonlinear processes working together; most of the above processes will occur in the generation of supercontinuum at some point. Chapter 5 describes how, through an understanding of supercontinuum dynamics, the bandwidths of supercontinua can be extended into blue and ultraviolet wavelength regions.

In bulk solid and gaseous nonlinear media, nonlinear frequency broadening of laser pulses was first observed in the late 60s and early 70s [61, 62]. However, as a practical light source, fibre-based continua were far more desirable, giving light guided in a fundamental fibre mode which can easily be used for further applications. In conventional optical fibres, a continuum spanning 180 nm was reported in 1976 by launching 10 ns pulses from a visible dye laser with a peak

power $>$ 1 kW into a 19.5 m section of fibre. The field of supercontinuum generation has been rejuvenated over the past 8 years with the advent of PCF [5, 57], where the ability to engineer significantly the fibre dispersion profile [21, 22] allowed the tailoring and enhancement of the contributing nonlinear mechanisms [63]. The first supercontinuum generation in PCF was reported by Ranka et al. in 2000 [64]. Here, continuum spanning from 390 nm to 1600 nm was generated in a highly nonlinear section of PCF pumped by 100 fs pulses from a Ti:Sapphire laser at 790 nm. One of the fields in which supercontinuum generation has readily found applications is that of frequency metrology [65, 66], where work with frequency combs generated by supercontinua led to one half of the Nobel prize being awarded to Hall and Hänsch in 2005.

Different techniques have been employed in order to enhance the bandwidth of supercontinua, particularly into the ultraviolet and visible regions of the electromagnetic spectrum. Techniques such as the use of dual pumps [67], intermodal mixing [68], fibre post processing [69] and fibre tapering [70] have all been reported in the last few years. However, the most common method of generating laboratory and commercial supercontinuum sources remains a single pump laser pumping a uniform fibre close to the zero dispersion wavelength generating continuum in the fundamental fibre mode. Although this method can be restrictive on bandwidth, the fibre is commercially available [71], and several different pump sources can be readily obtained and incorporated into a laboratory.

The dominant mechanisms for spectral broadening depend on the input pulse duration and whether the pulse pump is in the normal or anomalous dispersion regime. In the case of normal dispersion, the broadening is principally dominated by SPM and Raman scattering, whilst pumping in the anomalous dispersion regime gives rise to continua principally dominated by soliton-related dynamics. Similarly, the dependence on $\frac{\mathrm{d}I}{\mathrm{d}t}$ of SPM means that, for initially very short pulses, the SPM induced broadening can be very large. However, for the case of ns continua, the effects are minimal. The proximity of the pump to the zero dispersion wavelength is also necessary for degenerate FWM

to take place efficiently.

2.9 Summary

Important nonlinear effects have been described in this chapter, of particular importance for the work presented in chapters 4 and 5 are soliton dynamics. Before describing work carried out in nonlinear optics, to which we return in chapter 4, we first study the effects of modifying AS-PBGF claddings on the linear properties of guidance.

Chapter 3

The ring fibre

3.1 Introduction

The work presented in this chapter moves away from the nonlinear effects, described in the previous chapter, to show how modifications to the cladding structure of all-solid bandgap fibres can be used to reduce the losses when the fibres are bent. We will return to nonlinearity in the next chapter. All-solid photonic bandgap fibres (AS-PBGFs) consist of cladding structures comprised of two glasses, one with a slightly raised refractive index from the other, and a core usually formed from the lower index material [15, 16, 33]. They provide a useful structure in which to study bandgap guidance and the modal properties of the cladding. This is because, unlike in air-silica structures (which must be supported by connecting struts), the high index regions can be completely isolated from one another. This allows the cladding structure to be considered as an array of individual TIR-guiding cores supporting a set of guided modes, which is an easier concept to analyse (using the Anti-Resonant Reflecting Optical Waveguide (ARROW) model, see section 1.7 of chapter 1 [29–32]) than the complex high index "web" structure of air-silica bandgap fibres. Although

losses as low as 2 dB/km have now been reported [72], a serious limitation to unlocking potential uses for AS-PBGFs is that they suffer from very high bend losses [33] (a property which is negligible in air-silica bandgap fibres). During the course of this work, Birks et al. studied the bend loss mechanism in AS-PBGFs [73]. A summary of their findings will be reviewed as a basis for this chapter, after which we will present results in which the findings of Birks et al. were used to redesign the cladding structure of AS-PBGFs in order to reduce bend losses.

3.2 A review of bend losses in all solid bandgap fibres

This section contains a summary of work carried out during the course of this thesis in which I took no part. This work was carried out by Birks et al. [73] and is reproduced here as it is key to understanding my results presented later in the chapter.

An AS-PBGF was fabricated in order to study its losses when subject to bending. The starting materials for the fibre were pure silica canes and a germanium-doped multimode preform, drawn to canes, which would form the high-index regions. The manufacturer's specifications stated that the index profile of the germanium-doped canes was $\Delta n(r) = \Delta n_0[1 - (\frac{r}{r_\mathrm{d}})^{4.7}]$ where r_d is the radius and $\Delta n(r)$ is the refractive index contrast at a distance r from the centre of the rod. The maximum refractive index contrast between the high index inclusions and the background material, Δn_0, was 2.03%.

The high- and low-index canes were stacked alternately to form the cladding, and the central high-index cane was omitted to form the low-index core defect. The stack was then drawn down to preforms and then to fibre. The final dimensions of the fibre were $d/\Lambda = 0.44$ and $\Lambda = 15\,\mu$m (fig. 3.1a).

Light was coupled into the fundamental bandgap guided mode from a broadband supercontinuum source, and the output spectra for a straight fibre and for different bend radii (15 cm and 7.5 cm) were recorded on an OSA. The results are shown in fig. 3.1b. The transmission spectra in fig. 3.1 show that the degree of loss suffered due to bending was different for different bandgaps; in particular, the odd numbered bandgaps (1 being the fundamental, lowest frequency, bandgap) suffered less loss than the even numbered bandgaps. It was also observed that the losses were greater on the short wavelength edge of the bandgaps.

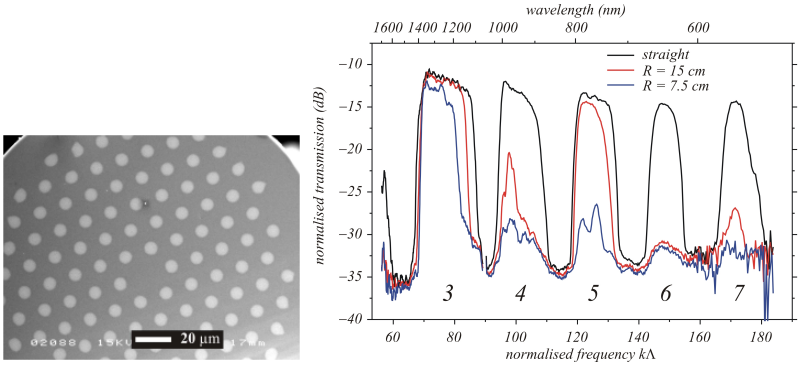

(a) (b)

Figure 3.1: An SEM image of the all-solid bandgap fibre used by Birks et al. is shown in (a). The dimensions of the fibre are $d/\Lambda = 0.44$ and $\Lambda = 15\,\mu$m. The transmission spectra through the fibre when illuminated with a broadband source are shown in (b). The individual bandgaps can be observed and are numbered. Transmission through sections of fibre which are straight and with different bend radii (15 cm and 7.5 cm) is shown.

The photonic density of states of the cladding array of high-index regions was also modelled as an infinite cladding array [74]; it is shown as a function of effective refractive index $n = \frac{\beta}{k_0}$ against normalised frequency $k\Lambda$ in fig. 3.2. The modes supported in the cladding are labelled as LP_{lm} and the effective index of the fundamental bandgap guided mode is shown in yellow. The bandgaps are numbered as in fig. 3.1.

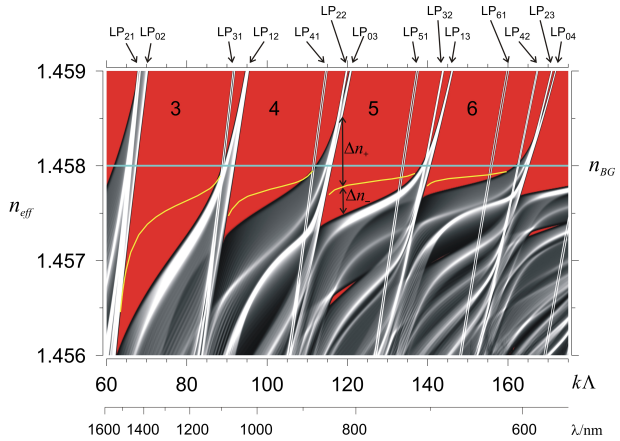

Figure 3.2: Modelled cladding photonic density of states plots shown as a function of effective refractive index against normalised frequency for the geometry of the experimental fibre. The red regions where there are no cladding modes form the low-loss bandgaps. They are numbered as in fig. 3.1b. The cut-off line is labelled n_{BG} and shown in light blue.

3.2.1 Why even and odd bandgaps are different

The mechanism identified as the cause of the high losses was analogous to the bend loss mechanism in conventional optical fibres. When a fibre is bent, the light travelling at the outside of the bend has to travel further than the light travelling on the inside of the bend to reach the same point. This can be considered to be equivalent to a straight fibre with a refractive index profile skewed across its diameter, with a gradient proportional to the magnitude of the bend radius in the direction of the bend as shown in fig. 3.3a and fig. 3.3b. The core radiation can now couple into a cladding mode with the same effective index, through resonant tunnelling, to a radiation caustic. As the bend diameter is increased, the index mismatch, Δn, between the fundamental core mode, n_{fm}, and the cladding, n_{cl}, is reduced. As a result of this, the radiation caustic moves closer to the core and increases the loss as the tunnelling distance is shorter. In the case of conventional optical fibres, this only happens centrifugally (on the outside of the bend) as the refractive index of the cladding is lowered on the inside of the bend. However in the case of AS-PBGFs, cladding modes exist which have a higher refractive index than that

of the the fundamental core mode, so as these are lowered on the inside of the bend they provide a second radiation caustic, which allows light to escape centripetally (on the inside of the bend) as well as centrifugally. The effective index mismatches between the nearest cladding modes and n_{fm}, above and below n_{fm} are labelled Δn_+ and Δn_- respectively in fig. 3.2 and fig. 3.3. It can be seen from fig. 3.2 that, across most of the width of the bandgap, Δn_- is significantly smaller than Δn_+, and that it decreases towards the higher frequency edges of the bandgap. Consequently, the bend loss in AS-PBGFs is mainly centrifugal and increases towards the blue edge of the bandgaps. The mismatch Δn_- is also noticeably smaller for the even-numbered bandgaps, accounting for the higher bend loss observed in these bandgaps, seen in fig. 3.1.

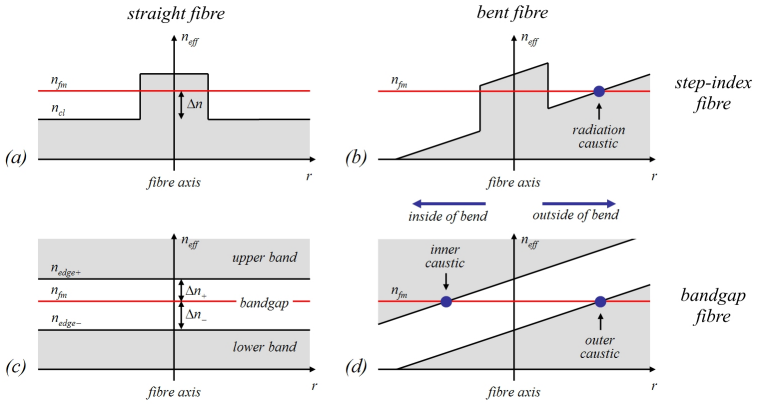

Figure 3.3: A schematic demonstration of bend loss mechanisms in conventional step index optical fibres (a), (b) and all-solid photonic bandgap fibres (c), (d). (a) and (c) show the effective refractive index profiles for straight sections of the fibres, whereas (b) and (d) show the effective refractive index profiles of bent sections of fibre.

Further investigation was carried out to establish why the 'depth' of the even bandgaps was shallower. The symmetry of the cladding modes which defined the edge of the bandgaps was considered. The circular nature of the high-index rods allows their supported modes to be thought of as the familiar LP_{lm} modes of conventional optical fibres, where the integers l and m describe the azimuthal and radial variations of the field in the rod. Arrays of these high-index regions form bands of supermodes as shown in fig. 3.2. The width of

the bands is defined by how strongly the individual modes couple together. Fig. 3.4 shows the intensity $|\Psi|^2$ of the modal field varying as a function of radius from the centre of a high index rod, for a set of modes with $l = 0, 1, 2, 3$ but a constant radial number $m = 2$. The low-l modes decay weakly into the background material (with the $l = 0$ mode not decaying at all) resulting in stronger coupling between these modes than between the higher-l modes. The low-l modes decay weakly for all values of m. The bands formed by these low-l modes are broader, so bandgaps where the edge of the gap is defined by a low-l mode will be shallower. Near field images of the cladding modes were observed, and modelling of the cladding modes at the band edges confirmed that the even bandgaps were defined by a low-l cladding mode at the edge.

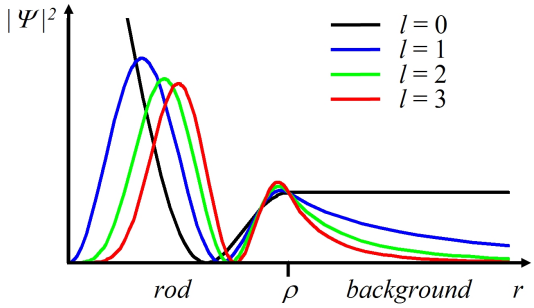

Figure 3.4: Intensity distributions as a function of radius, r, for the $m = 2$ family of modes ($l = 0, 1, 2, 3$). The lower-l modes can be seen to decay weakly into the background material, $r > \rho$, where ρ is the radius of the high-index rod.

3.3 Cladding restructuring

The remainder of the chapter describes work carried out by myself, building on the findings of Birks et al.

A natural suggestion arising from the work of Birks et al. is to restructure the fibre cladding in order to suppress these troublesome low-l modes, in particular by removing material from the centre of the high index regions so they have

the appearance of rings in the fibre cross section, as shown in fig. 3.5. This will result in the higher-order radial modes (higher m) being swept away to higher frequencies, as there is "less room" for them where they would naturally exist, leaving only the $m = 1$ modes relatively undisturbed. Fig. 3.5 shows two modelled modes of a step-index fibre: one $m = 1$ mode, LP_{61}, and one $m > 1$ mode, LP_{52}; the yellow circle marks the boundary between the core and the background material. If the high-index material was removed from inside the red circle, it can clearly be seen that there would be little modification to the LP_{61} mode as the majority of the intensity distribution still lies within the high index region. However, the majority of the field of the LP_{52} mode would lie within the removed region so would be forced to adapt.

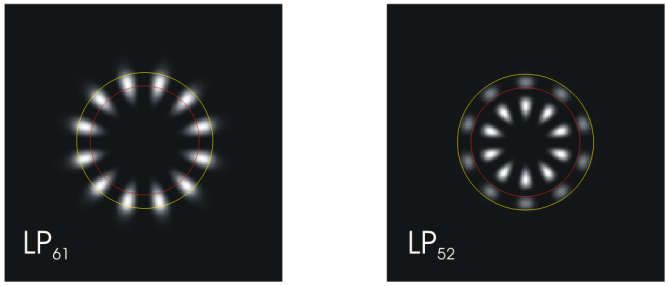

Figure 3.5: Modelled electric field intensity patterns for the LP_{61} and LP_{52} modes of a step-index fibre of core radius ρ. The yellow circle at $r = \rho$ shows the boundary between the high-index core and the cladding region, whereas the red circle is at $r = 0.8\rho$. It can clearly be seen that the removal of the high index material inside the red region would leave the LP_{61} mode relatively unperturbed but would significantly alter the LP_{52} mode.

3.4 Modelling

In order to demonstrate the effects of moving from rods to thin rings, modelling was carried out by G. J. Pearce using the fully-vectorial fixed-frequency plane-wave method [74]. A series of density of states (DOS) for cladding structures was plotted, with the high-index inclusions varying from solid rods to thin

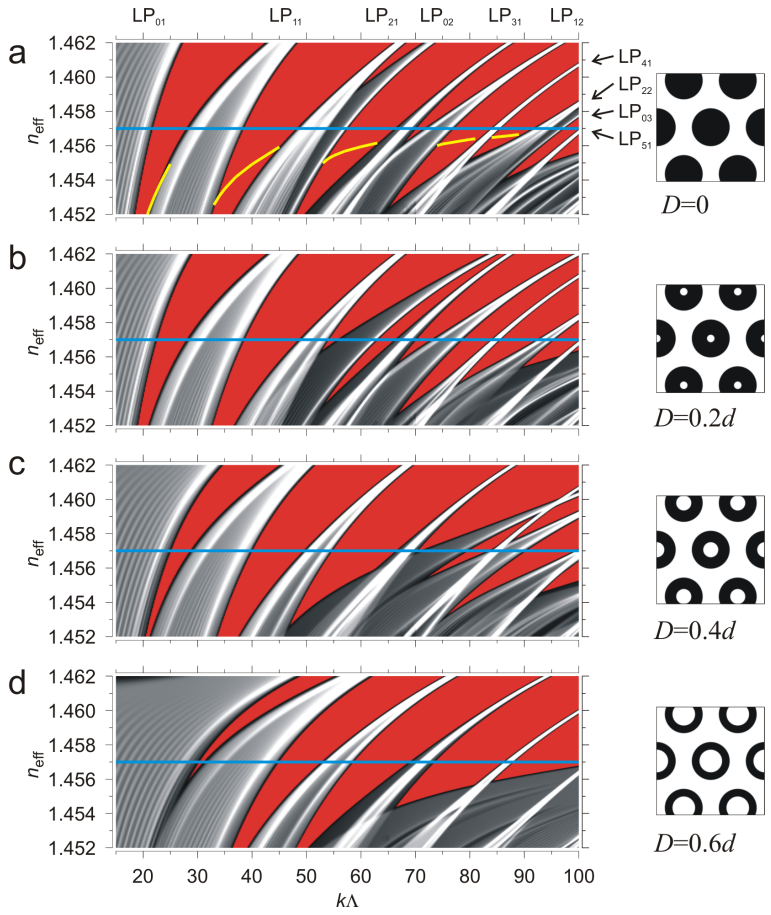

Figure 3.6: Photonic density of states plots as a function of effective index against normalised frequency for a triangular array of high-index inclusions in a pure, undoped silica background of index $n = 1.457$, with $\Delta n = 1.09\%$. The series shows solid rods in (a) progressing to an inner diameter $D = 0.6d$ in (d). Specific guided modes are labelled in (a) and as material is removed they can be followed as they are swept away. The fundamental bandgap guided mode is shown in yellow in (a).

rings (fig. 3.6 and fig. 3.7). The plots shown on the left in fig. 3.6 and fig. 3.7 show the beginning of the evolution from rods, with the effective index of the fundamental core mode shown in yellow in the first case. Several of the cladding modes are labelled and can be seen to shift to higher frequencies as more high index material is removed, as would be expected from any process which reduces the effective V-values. The inserts show schematically what has been removed. As the end of the series is approached, fig. 3.7, only the modes

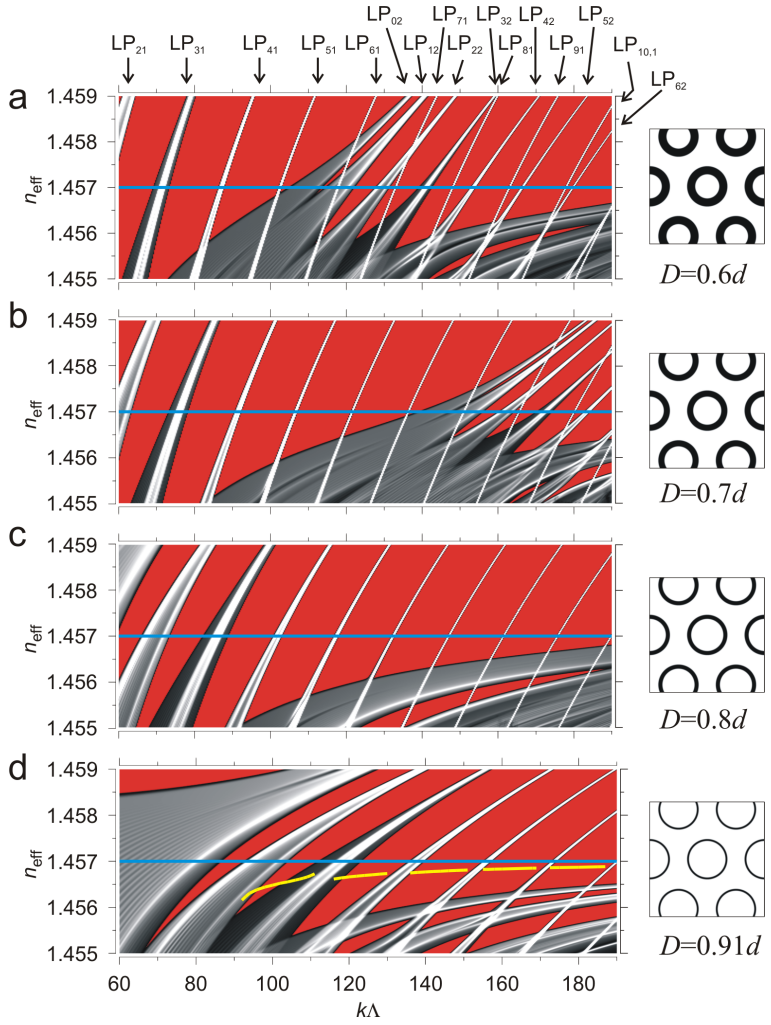

Figure 3.7: Photonic density of states plots as shown in fig. 3.6, but for a range of rings with inner to outer diameter ratio of 0.6 to 0.91. The diameter of the thinnest ring was chosen to closely match our experimental case. Note the scale changes from fig. 3.6. The structure with $D/d = 0.6$ has been repeated for clarity.

with $m = 1$, $l > 1$ remain relatively unperturbed, with all the $m > 1$ modes dramatically shifted to higher frequencies (note the the change in axis scales between fig. 3.6 and fig. 3.7, fig. 3.6d and fig. 3.7a are the same structure). The final case is close to our experimental fibre detailed in the next section, where the inner to outer diameter ratio is 0.91. At this point, it can be seen that the rings have become so thin that even the $m = 1$ modes are beginning

to be displaced. The effective index of the fundamental bandgap guided mode is again shown in our final case.

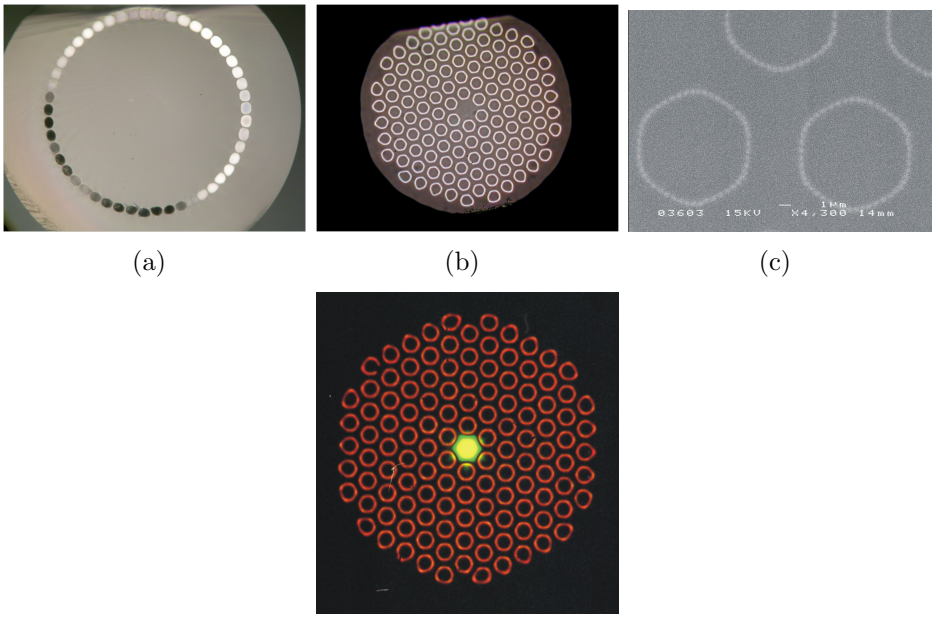

(a) (b) (c)

(d)

Figure 3.8: (a) shows an optical micrograph of a unit cane, with the individual high-index rods still visible, and (b) shows an optical micrograph of the final ring fibre, with a core of approximately 15 μm in diameter. (c) shows a scanning electron micrograph of the cladding region of the final fibre; even here the individual high index rods are still visible. (d) shows a near field image of the output face of a ring fibre slightly smaller than the one reported in the experimental section.

3.5 Fabrication

Our ring cladding was created using a multiple stacking process. Our starting material was a set of germanium-doped silica canes with a thin pure silica coating (total diameter 0.82 mm, diameter ratio 0.88). These rods were stacked in a circular array between a large solid silica rod and an outer silica tube. This stack was drawn to preforms of 1.52 mm diameter and formed the unit cell of

our ring cladding (fig. 3.8a). The canes were then stacked in a close-packed array, replacing the central cane with a pure silica cane in order to form the low index core. The stack was drawn to preforms and then to fibre. Each ring of the final fibre is therefore actually a ring of closely spaced rods separated by around 0.6 μm, fig. 3.8a. The diameter of the core in the final fibre was $\approx$15 μm and the diameter of the ring to pitch ratio, d/Λ, of the final fibre was 0.72 with a ring thickness of $\approx 0.05d$. The effective refractive index contrast of the ring was estimated to be 1.09% using the average index of the starting rod. The slightly hexagonal shape of the rings is a consiquence of the slow drawing speed, which was required in order to collapse the interstitial holes, as can be seen in fig. 3.8c.

3.6 Analysis

In order to characterise the ring fibre, a 90 cm section was fusion-spliced to a section of 12 μm core endlessly single-mode fibre [6], to obtain efficient coupling into the fundamental bandgap-guided core mode. Light from a broadband supercontinuum source [63] was coupled into the endlessly single-mode fibre and the emerging light from the core of the ring fibre was analysed using an optical spectrum analyser. The transmission spectra shown in fig. 3.9a are those for straight (blue) and bent (red, 1 turn of diameter 7.5 cm) sections of the ring fibre. In order to compare the performance of the ring fibre with that of a more conventionally fabricated "rod" AS-PBGF (corresponding to the first case of our simulations in fig. 3.6a), we have performed similar experiments on such a "rod fibre" as well. The characteristics of the rod fibre were: a slightly higher refractive index contrast at 2.03%, a pitch of $\approx$15 μm and $d/\Lambda \approx 0.7$. The transmission spectra recorded in a similar way using the rod fibre are shown in fig. 3.9b. By careful identification of the near field images of the cladding modes using a CCD camera (see examples in fig. 3.10), we were able to identify unambiguously specific high-l mode crossings in the two fibres, which manifest themselves as sharp dips in the straight transmission spectra.

The number of lobes identified in each mode (= $2l$) has been labelled in fig. 3.9.

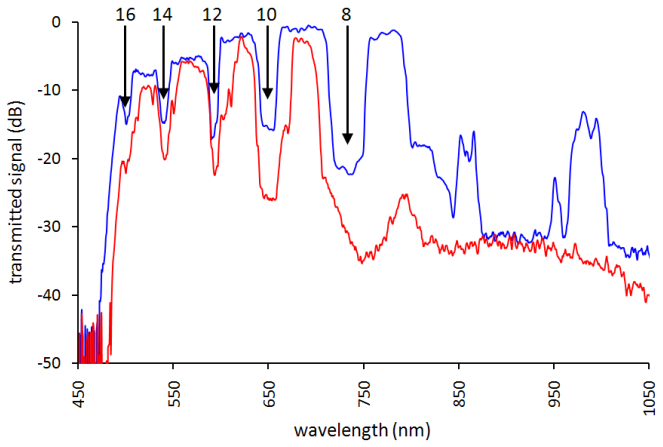

(a)

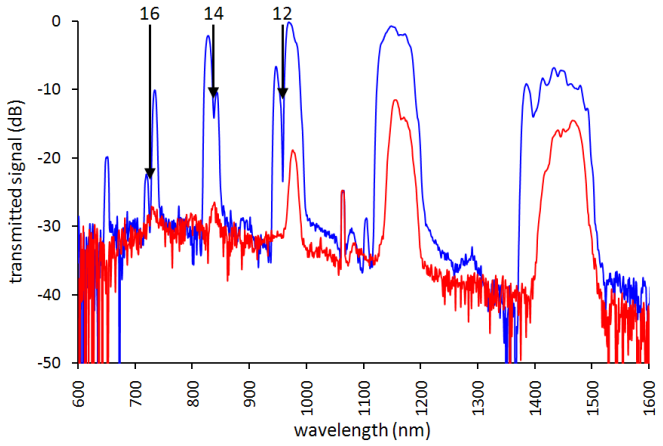

(b)

Figure 3.9: Transmission spectra for (a) the ring fibre and (b) a rod fibre with similar pitch and d/Λ. The overall spectral shape, including the sharp edge in the ring fibre at 480 nm, is due to the supercontinuum source used to illuminate the fibre. The blue traces are for transmission through straight sections of fibre and the red traces are for a single turn of diameter 7.5 cm. The numbers indicate the number of lobes measured in the crossings at the indicated wavelengths. The peak at 1064 nm in (b) is again due to the supercontinuum source.

For the straight rod and ring fibres, a series of low-loss transmission windows can be seen corresponding to the photonic bandgaps. The changes in the

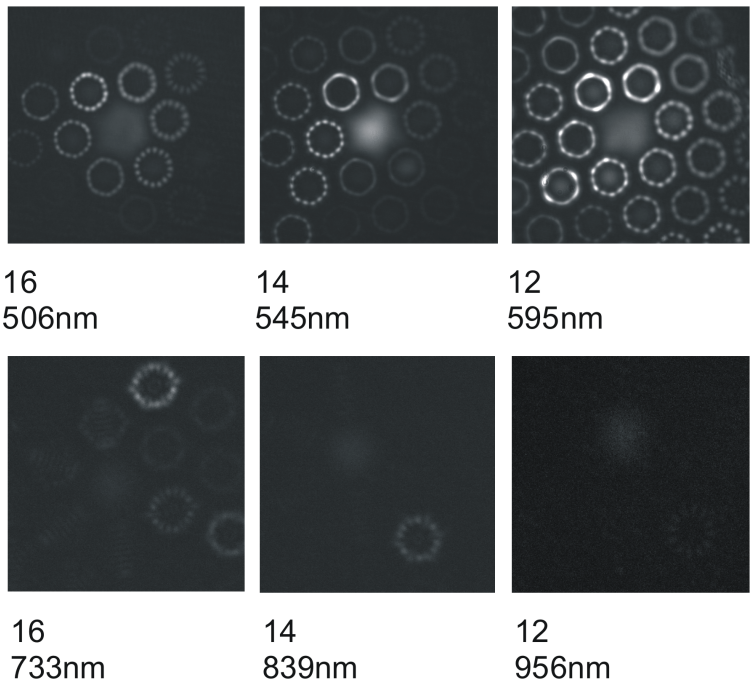

Figure 3.10: Near field images of unconfined modes excited by leakage from the core between the bandgaps in the ring fibre (top) and a rod fibre (bottom). The same high-l modes are observed for both ($l = 6, 7, 8$ indicated under each image by the number of bright lobes in the mode)

cladding mode structure shown in the DOS plots of fig. 3.6 and fig. 3.7 lead to significant changes in the locations and widths of the bands. The broad high attenuation features corresponding to large mode crossings of multiple modes in the rod fibre are eliminated in favour of the sharp crossings of the $m = 1$ modes in the ring fibre. The lowest order bandgaps (longest wavelength) in the ring fibre do not provide robust guidance; this is to be expected from our DOS plots as Δn is small in these regions. The crossings of the $l = 6, 7$ and 8 modes in the rod fibre can be seen as the narrow attenuation features marked in fig. 3.9b. However, the shape of the transmission spectrum is dominated by much broader features due to the crossings of the lower-l cladding modes. In the ring fibre, these features have been swept away, leaving just the sharp loss regions associated with the same high-l modes. The higher order bandgaps in the ring fibre do indeed exhibit less loss when bent compared to those of the

rod fibre. It should also be noted that the effective refractive index contrast in the rod fibre is also larger by a factor of around 2. The improvement in bend loss performance is therefore marked, despite the bandgaps being shallower. This improvement can be attributed to the very weak coupling between the high-l cladding modes and the fundamental guided core mode.

3.7 Conclusions

We have modelled, fabricated and characterised an AS-PBGF with a 2d ring matrix cladding, with the intention of reducing bend loss. This is achieved by suppressing higher order radial cladding modes, thereby reducing bend loss as the remaining lower order radial cladding modes couple weakly to the fundamental guided core mode. We have experimentally verified the improved performance by directly comparing our ring fibre with a similar rod fibre. Furthermore, our fabrication technique enables the fabrication of novel cladding structures, where the unit cell of the cladding can be engineered to have enhanced properties. This procedure has already led to the design of other AS-PBGFs with enhanced characteristics [36].

3.8 Nonlinear optics in all-solid photonic bandgap fibres

AS-PBGFs are not ideal fibres for the study of nonlinear effects. This is due to the relatively large effective core areas, leading to a reduction in the nonlinear coefficient when compared with step index PCFs. In addition the bandgap nature of the guidance limits large portions of the available spectrum. SPM, soliton propagation and the Raman self-frequency shift were however, demonstrated by Fuerbach et al. [75] in a solid core PCF with the holes filled

with a high index liquid to form a bandgap guiding structure. Recently it was reported that AS-PBGFs can be used to confine the power of a generated supercontinuum to a bandgap of a few hundred nanometres giving a relatively narrow continuum, but with high spectral density [76]. Further to this work, it was shown by Bértourné et al. [77] that a soliton self frequency shifting to the edge of the bandgap ceases to shift into the high loss region confining the energy in the bandgap. So, although not the perfect fibre for nonlinear studies, AS-PBGFs are finding their niche. In the following chapters we will explore nonlinear effects in TIR guiding PCFs, a far more common fibre for observing nonlinear propagation.

Chapter 4

Pulse compression

4.1 Introduction

In this chapter we move into the nonlinear regime to explore solitonic methods of optical pulse compression. Optical pulse compression is an important technique for many optical systems which require ultra-short bandwidth-limited pulses for specific applications. In particular, the observation of many nonlinear effects relies on the duration of the pulse and become strong when the duration is very short. Pulse compression is generally achieved in systems such as Titanium Sapphire oscillators by introducing a selective degree of linear chirp over a pulse of given bandwidth, which is then compensated for by a set of diffraction gratings. This technique is cumbersome and requires a great deal of effort in initially aligning and maintaining the system. In contrast, compression techniques involving solitonic compression can be achieved by launching light into one section of optical fibre with the correct characteristics. These techniques are becoming more important as the emerging market for high-power fibre lasers becomes established.

Two methods of solitonic pulse compression which rely on different aspects of soliton propagation exist: adiabatic soliton compression (ASC) and soliton effect compression (SEC). These two methods can act alone or in combination to generate near transform-limited pulses of the order of a few tens of femtoseconds. ASC uses the fact that fundamental solitons adjust adiabatically to small variations in the waveguide properties or in the soliton energy, and adjust their duration accordingly. SEC uses the property of higher order solitons that they "breathe" over the duration of a soliton length. At a certain point in the breathing cycle, the soliton undergoes large temporal compression. If the nonlinear medium is terminated at this point, very short pulses can be generated. In this chapter, we will discuss using these methods in PCFs and present work carried out in collaboration with Imperial College London.

4.1.1 Adiabatic soliton compression

ASC relies on the the fact that a fundamental soliton propagating in an optical fibre will adjust its duration, τ, if the characteristics of the waveguide or the energy of the soliton itself are varied slowly with respect to the soliton length [78]. The duration of a fundamental solition at its full-width half-maximum, τ_{fwhm}, is given by

$$\tau_{\mathrm{fwhm}} = 1.76\frac{\lambda^3 D A_{\mathrm{eff}}}{2\pi^2 c n_2 E_{\mathrm{sol}}} \tag{4.1}$$

where λ is the wavelength, D is the group velocity dispersion, A_{eff} is the effective core area, n_2 is the nonlinear refractive index and E_{sol} is the soliton energy. If any of the parameters on the right-hand side of 4.1 are varied slowly with respect to the soliton length, then τ_{fwhm} will adjust to compensate for this change, compressing or lengthening the pulse appropriately. The parameters that can be readily varied along the length of an optical fibre are D, A_{eff} and E_{sol}. It is clear from equation 4.1 that a decrease in dispersion or effective core

area will act to compress the pulse, whereas a reduction in the soliton energy (for example through loss) will broaden the pulse.

ASC in conventional optical fibres with dispersion decreasing along their length was reported in the early 1990s by Chernikov and Mamyshev [78, 79]. Temporal variations in solitons in the presence of media with gain or loss were also investigated by Smith and Mollenaur in 1989 [80]. In ref. 79 conventional optical fibres were tapered during the drawing process to give them dispersion profiles varying along their length. In a 100 m taper, a 630 fs pulse from a ring cavity erbium fibre laser was compressed to 115 fs giving a factor of 5.5 compression. The dispersion varied from 10 to 1.4 ps nm^{-1} km^{-1} at 1550 nm. A second longer taper was also fabricated for picosecond pulse compression. Here the dispersion varied from 10 to 0.5 ps nm^{-1} km^{-1} over a length of 1.7 km, and 230 fs pulses were obtained from transform-limited 3.5 ps pulses, again at 1550 nm. This demonstrated a factor of 16 compression for a factor of 17.5 decrease in dispersion, indicating a near optimal fibre design for picosecond pulse compression.

In these cases, the intrinsic limitation on wavelength of the pulses which could be compressed is the extent of the anomalous dispersion region. In conventional optical fibres, the anomalous dispersion regime cannot be greatly modified from that of bulk silica (above 1.3 μm) and is therefore restricted to wavelengths where λ >1.3 μm. This leaves little scope for the exploitation of this technique for use with other sources. A particular region of interest is around the 1064 nm, band where recent commercial activity has produced advances in high power Yb^{3+} fibre lasers for applications such as spectrally very bright supercontinuum sources [81, 82].

Through changing the size and separation of the air holes, it is possible to modify strongly the dispersion profile of PCFs [1, 5, 21, 22]. The fact that it is possible to shift the anomalous dispersion into the visible wavelength region [22] suggests that they would be ideal for observing large compression ratios below 1.3 μm, in particular the 1064 nm region. ASC at 1064 nm in

PCFs was reported by Tse et al. [83] in 2006 during the course of our work; however, the high loss of the taper (150 dB/km) limited the taper length to 8 m. The modelled dispersion profiles for their work indicated a factor of ≈2 decrease in dispersion between the input and output ends of the taper from 5.4 to 2.3 ps nm^{-1} km^{-1}, allowing the compression of 130 fs pulses to 60 fs. The length is, however, short when compared to the soliton length, which could indicate that ASC was not acting alone and may have been assisted by SEC. The loss of this taper is extremely high, and reducing it would allow a much greater ratio between the input and output dispersion. No mention is made as to the underlying cause of the unusually high loss, for example, whether it was due to the taper or if it could be improved by better fabrication. It is possible to engineer dispersions at 1064 nm from as high as a few hundred ps nm^{-1} km^{-1} to as low as 0 ps nm^{-1} km^{-1}. In the case where the dispersion at the output approaches zero, the pulse duration would be limited by the third order dispersion, β_3. It is therefore favourable to keep β_3 as low as possible by designing tapers with zero slope in β_2 in the wavelength region of compression.

4.1.2 Soliton effect compression

SEC arises from the natural dynamics of higher order solitons, $N > 1$ [43, 84]. The temporal characteristics of a higher order solitons evolve as they propagate, compressing an lengthening with the solitons returning to their original temporal profiles after one soliton period. Although this is only true in the femtosecond regime if the effects of higher order dispersion and Raman scattering are neglected. In each period there is a large temporal compression, with associated spectral broadening. If the nonlinear medium is terminated at the point of maximum compression, the pulse generated can be much shorter than the input pulse. In practice, in the femtosecond regime, the periodic evolution of higher order solitons does not occur as the effects of Raman scattering and the dispersion slope cannot be ignored. In this case, the soliton does not go through cycles, as the initial compression of the pulse causes the pulse to

break up into fundamental solitons. This effect is known as soliton fission. As the initial compression can be large high, compression ratios can be achieved. Indeed, experiments by Foster et al. produced a 6.8 fs pulse from an initial 70 fs input pulse in a 2 mm section of photonic crystal fibre [85]. An empirical relation for the optimal distance at which the maximum compression occurs z_{opt} in terms of the soliton order N is given by [43]

$$\frac{z_{\text{opt}}}{L_{\text{D}}} \approx \frac{0.32}{N} + \frac{1.1}{N^2}, \tag{4.2}$$

with the compression factor $\frac{\tau_{\text{in}}}{\tau_{\text{out}}}$ approximated by

$$F_{\text{c}} \approx 4.1N, \tag{4.3}$$

where L_{D} is the dispersion length.

4.2 Adiabatic soliton compression in dispersion-decreasing photonic crystal fibre tapers

We now move on to discuss the design and fabrication of improved tapers for ASC using a picosecond fibre laser at 1064 nm as a pump.

4.2.1 Design and fabrication

To choose the correct taper profile, linear modelling of the dispersion curves for several fibre designs was carried out using the code CUDOS MOF, available from CUDOS at the University of Sydney [86, 87]. The input and output pro-

files were chosen with the dispersion assumed to vary linearly between them. The design was chosen to have a large variation (greater than a factor of 10 decrease) in dispersion between the input and output ends of the taper, in order to obtain a large compression ratio. This was achieved by engineering the dispersion at the output to be as close to zero as possible; however, the slope of the dispersion should also be kept as low as possible, as the maximum compression ratio would almost certainly be limited by third order dispersion [42, 78]. Third order dispersion relates to the slope of the second order dispersion, so as a broadens spectrally, as it pulse compresses temporally, different parts of the pulse will begin to experience different values of dispersion. Several fibre designs for the input and output were modelled, varying the pitch and hole size in small increments to find appropriate designs. Fig. 4.1a shows the variation of d/Λ ratio for a fixed Λ of 1.30 μm and fig. 4.1b shows variation in Λ for a fixed d/Λ ratio of 0.50. It is clear, from fig. 4.1 how small variations in the hole size or separation of the fibre affect the dispersion, in both slope and magnitude, in the wavelength region close to 1064 nm. Over the range of values modelled, decreasing Λ decreases the overall dispersion, shifting the region of zero slope to shorter wavelengths, whereas decreasing the d/Λ ratio decreases the overall dispersion but shifts the region of zero slope only slightly to shorter wavelengths. In practice, accurate tapering of the fibre holes is difficult to achieve when the required changes are $>1\,\mu$m.

The modelled dispersion curves shown in fig. 4.1c are for an example taper with input dimensions of Λ =1.4 μm and d/Λ =0.55 (shown in green) and output dimensions of Λ =1.3 μm and d/Λ =0.47 (shown in red). The dispersion at 1064 nm varies from 40 to 4 ps nm^{-1} km^{-1}, which indicates that a factor of ≈ 10 in compression should be achievable in a taper with these characteristics.

The chosen dispersion profiles have dimensions similar to those in fig. 4.1c. It was required that Λ vary from 1.4 to 1.3 μm and the d/Λ ratio vary from 0.55 to 0.47. The decrease in Λ can be achieved by reducing the outer diameter of the fibre, with which Λ scales linearly. In practice this was done by stopping the preform feed whilst maintaining a constant fibre drawing speed during the

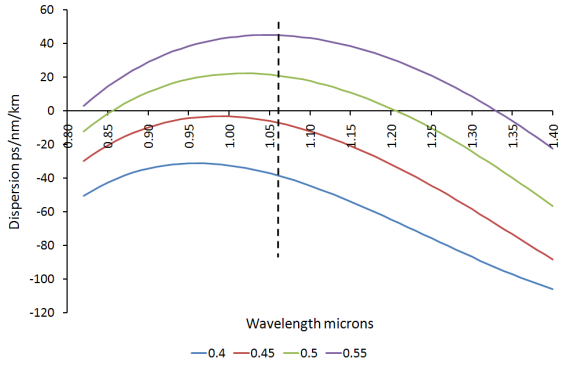

(a)

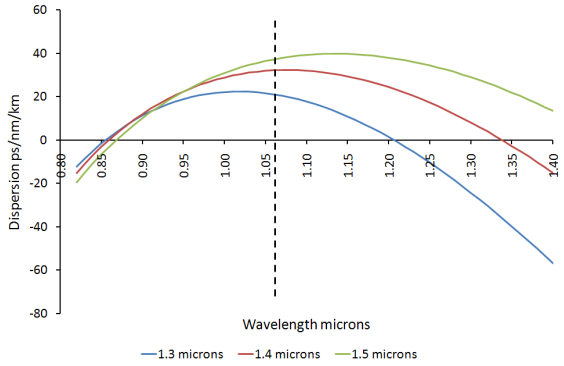

(b)

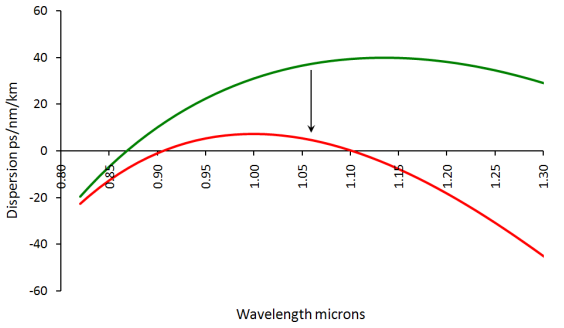

(c)

Figure 4.1: (a) Modelled dispersion curves for a fixed Λ =1.3 μm with $d/\Lambda = 0.40, 0.45, 0.50, 0.55$. (b) Modelled dispersion curves for a fixed d/Λ =0.55 with Λ =1.3, 1.4 and 1.5 μm. (c) Modelled dispersion curves for a taper with Λ varying from 1.4 to 1.3 μm and d/Λ varying from 0.55 to 0.47. The dispersion change between the input (green) and output (red) at 1064 nm is a factor of approximately 10.

final fibre draw. The reduction in the d/Λ ratio was achieved by reducing the pressure applied to the cladding holes of the preform. Both of these methods give little control over the final output dispersion profile so, during the taper production, the outer diameter was tapered further than required so the output end could be cut back until the correct final dispersion profile was found. During each taper run, two tapers were formed: the initial taper when the preform feed was stopped, and a second taper when the feed was restarted and the hole pressure returned back to its original value.

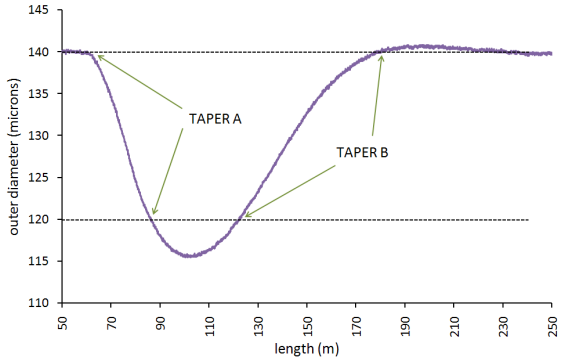

Figure 4.2: Taper draw data showing the variation in outer diameter with length. The taper formed from 140 μm to 120 μm is labelled taper A and the second taper, from 120 μm back to 140 μm, is marked taper B.

Fig. 4.2 shows the variation of the fibre outer diameter with distance. The initial parameters were allowed to settle before the feed was stopped and the pressure dropped, indicated by the first arrow in fig. 4.2. This point was marked on the fibre drum with masking tape and the fibre allowed to taper. The distance from the furnace to the fibre drum was measured to be 6 m. As the circumference of the drum was known to be 1 m, six turns of the drum were counted after the parameters changed before the marker was placed. When the outer diameter reached 120 μm (the second arrow in fig. 4.2), forming taper A, the pressure was then returned to 15.5 kPa and the preform feed restarted. The effects of varying the draw parameters is not instantaneous, so the fibre continued to taper before returning to 120 μm diameter and forming a second longer taper marked as taper B.

The method of forming fibre tapers by stopping the feed is similar to that reported by Kudlinski et al. [70] except that, to form shorter tapers for supercontinuum generation, the preform feed was retracted slightly. Our tapers needed to be several soliton lengths in order to allow a soliton to form and adjust to the varying dispersion along the taper length. The soliton length, z_0, defined in section 2.6 is given by

$$z_0 = \frac{\pi}{2} L_{\mathrm{D}} \approx \frac{\tau_{\mathrm{fwhm}}^2}{2\,|\beta_2|}. \tag{4.4}$$

As it scales with the square of τ_{fwhm}, pulse compression from longer pulses therefore requires longer tapers in order to allow the parameters to vary slowly. The length of our tapers can be seen to be 23 m for taper A and 54 m for taper B from fig. 4.2. Being over twice the length of taper A, taper B could potentially suffer over twice the loss; however, having a slower variation in dispersion over the length would allow a fundamental soliton to form fully and then be compressed by ASC alone.

4.2.2 Characterisation

Scanning Electron Micrograph (SEM) images of the input and output ends of the tapers were taken and are shown in fig. 4.3. Λ varies from 1.44 to 1.25 μm with d/Λ going from 0.52 to 0.42 in taper A. For taper B, Λ varies from 1.48 to 1.20 μm and d/Λ changes from 0.55 to 0.45. Both the core sizes varied from 2.2 to 2.0 μm, giving a small increase in γ which would aid the compression. The dispersion profiles were measured using the interferometric method outlined in ref. 88 and are shown in fig. 4.3. The dispersion at the output end of taper A was found to be in the normal regime (fig. 4.3c), so a two metre section was cut off and the dispersion remeasured. This was repeated until the dispersion was close to zero at 1064 nm, but was still normal. The length of the taper was now 17 m. All of the cut-back dispersion profiles are shown. The input

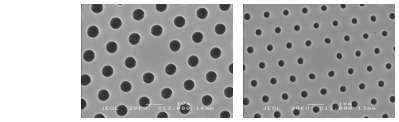

(a) (b)

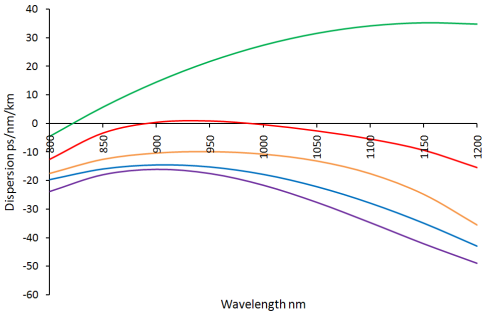

(c)

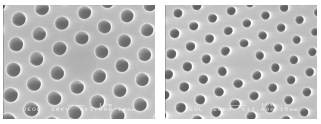

(d) (e)

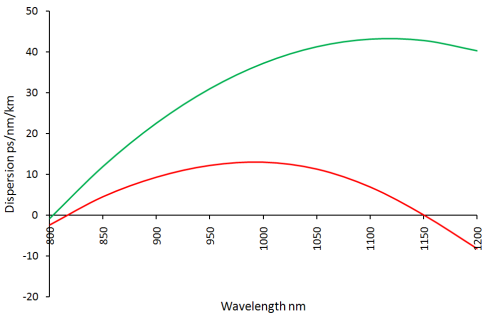

(f)

Figure 4.3: Scanning electron micrograph images and measured dispersion curves for the two tapers. (a) and (b) show the input and output of taper A respectively. (c) shows the dispersion curves for the input (green) and output (red) of taper A. Several 2 m cutbacks were made on the output of taper A, and the dispersion curve for each one is shown in purple, blue, orange and red for taper lengths of 23, 21, 19 and 17 m respectively. (d) and (e) show input and output images of taper B, with the corresponding dispersion curves (input-green and output-red) shown in (f).

dispersion value at 1064 nm was 33 ps nm^{-1} km^{-1}. The dispersion at 1064 nm in taper B was found to vary from 40 to 10 ps nm^{-1} km^{-1} (fig. 4.3f). With these ratios, taper A should give a large compression, whereas taper B should give approximately a factor of four in temporal compression.

4.2.3 Experiment

This section details the experiment carried out using a fibre grating compressor setup as a pump source for the tapers, carried out by J. C. Travers at Imperial College, London. The fibre grating compressor was set up as shown in fig. 4.4. Pulses with a duration of 6 ps were taken from a mode-locked ytterbium fibre laser and amplified by an ytterbium-doped fibre amplifier. These were then passed through a section of normally dispersive polarisation-maintaining fibre to apply a selective (by changing the length of the fibre) degree of approximately linear chirp to the pulses. Complete compensation for the chirp was then achieved by varying the separation of a transmission grating pair. This setup allowed the production of approximately bandwidth-limited pulses, time bandwidth product < 0.75, tunable between 100 and 900 fs. The pulse energy coupled into the tapers was varied by means of a half-wave plate placed before the polarised transmission gratings, with a second half-wave plate placed before the input of the taper to control the polarisation of the input pulses. The input pulse duration was adjusted for the highest compression ratio for each of the pulses. For taper A, 655 fs pulses were used; for taper B, 830 fs pulses were used.

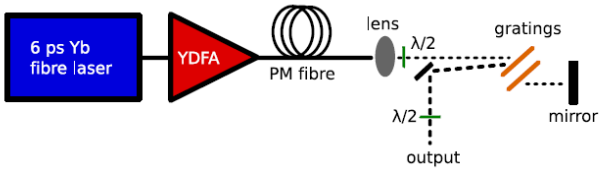

Figure 4.4: Experimental setup for pumping the fibre tapers. The ytterbium-doped fibre amplifier is labelled YDFA.

The pulses from both tapers were recorded spectrally on an OSA and temporally on an autocorrelator, with the input and output powers also recorded. The results for taper A and taper B can be seen in fig. 4.5 and fig. 4.6 respectively.

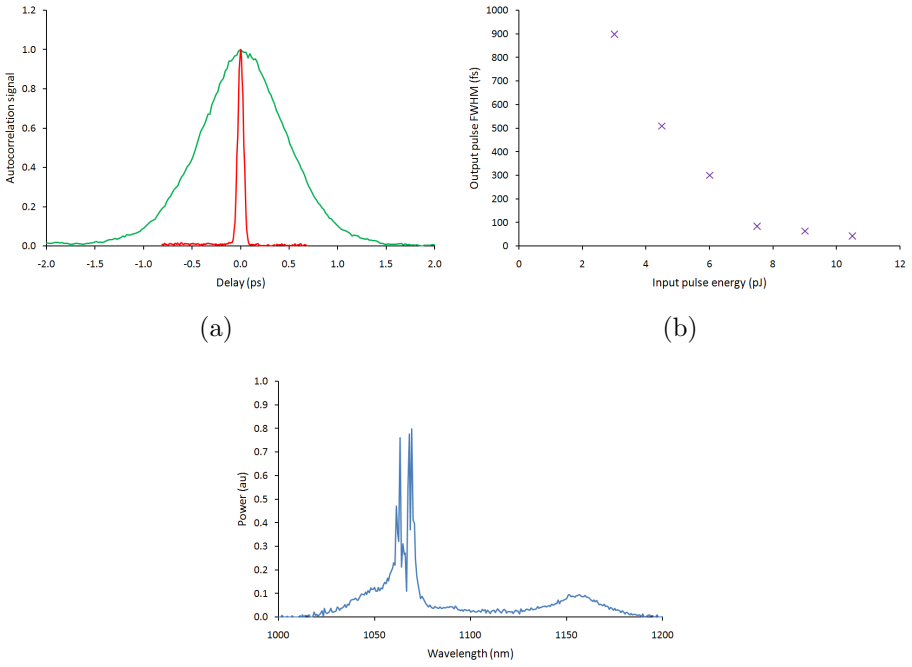

(a) (b)

(c)

Figure 4.5: Results for taper A. (a) shows autocorrelations of the input (655 fs, green) and output (43 fs, red) pulses. (b) shows the output pulse duration as a function of input pulse energy for an input pulse duration of 655 fs. (c) shows the output spectrum for the 43 fs (input energy 10.5 pJ) pulse shown in (a).

For taper A, a maximum compression ratio of 15 was observed from 655 fs to 43 fs at the full-width half-maximum. However, the soliton length for this input pulse was calculated to be 11 m; therefore, a taper length of 17 m was insufficient for ASC alone. The large compression ratio has therefore been attributed to the combined effects of SEC and ASC. The optimal length for SEC from an $N = 2$ soliton (the optimal length decreases with N, equation 4.2) was calculated to be 4 m, so it could not be acting alone. A small dispersive component was observed spectrally at around 1160 nm; this was attributed to the output dispersion of the taper becoming slightly normal at the end of the

taper.

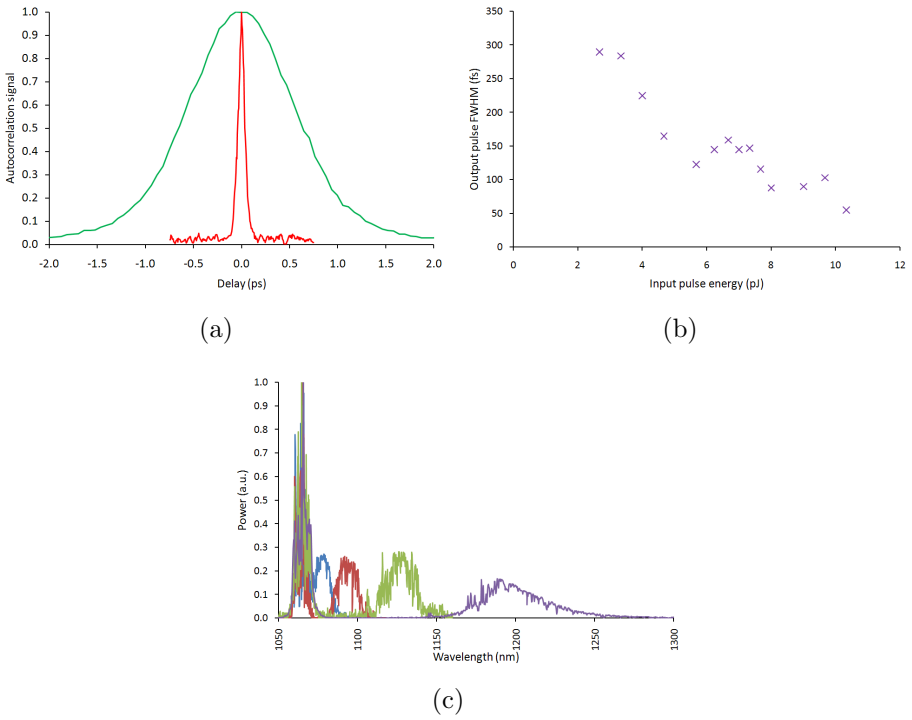

Figure 4.6: Results for taper B. (a) shows autocorrelations of the input (830 fs, green) and output (55 fs, red) pulses. (b) shows the output pulse duration as a function of input pulse energy for an input pulse duration of 830 fs. (c) shows output spectra for input pulse energies of 5.0 pJ (blue), 5.6 pJ (red),7.4 pJ (green) and 10.2 pJ (purple). The Raman self frequency shift for higher powers can clearly be seen.

The results for taper B are shown in fig. 4.6. A 55 fs output pulse was generated from a 830 fs input pulse; a factor of 15 compression. The time bandwidth product calculated from fig. 4.6a and fig. 4.6c was 0.31. This is a larger compression ratio than the dispersion ratio of 4 would indicate to be possible. To understand fully how such a large compression was achieved, we must look at the spectral results (fig. 4.6c). Here, for increasing power, a large spectral shift towards longer wavelengths is observed, due to Raman self scattering. The final output pulse is centered just below 1200 nm. Fig. 4.3f shows that the dispersion at this point is again close to zero, so the wavelength shift has significantly aided the compression. Soliton compression using wavelength

shifting solitons has been demonstrated in uniform fibres [89]. In addition to the Raman shift with power, fig. 4.6b shows that the pulse does not continually compress with increasing power, there are regions where it broadens, by ≈ 50 fs, before compressing again. This maybe due to the residual pump distorting the autocorrelation measurements, however, the Raman shift could also be playing a part. 4.4 shows that $\tau_{\text{fwhm}} \propto \lambda^3$, this may lead to a pulse that has a larger wavelength shift but still not experienced a large variation in dispersion lengthening temporally. This lengthening is not seen in the date shown for taper A in fig. 4.5b, however, as well as the Raman shift being significantly smaller, the amount of data points is significantly less for similar pulse energies than in fig. 4.6b. It should also be noted that the pulse duration scale ranges from 0 to 1000 fs in fig. 4.5b and from 0 to 350 fs in fig. 4.6b, on the larger scale the compression would appear smoother for taper B.

4.2.4 Conclusions

We have demonstrated the use of dispersion-decreasing PCF tapers in order to compress optical pulses. A maximum compression factor of 15 at 1064 nm was achieved in two tapers, with pulses as short as 43 fs generated in one of the tapers. As the soliton length for the input pulse is too short in this taper for ASC to act alone, the total compression is attributed to the combined contributions of ASC and SEC. The compression in these tapers appears to be limited by the extent of the anomalous dispersion region. Better control over the fabrication could lead to shorter pulses. The ultimate limit for this type of tapers is most likely to be third order dispersion, which will begin to act against the compression when the second order dispersion becomes close to zero [42, 78]. This method could be used to form ultra-short pulses in high power fibre lasers.

4.3 Further work

The simplest improvement that would allow better fabrication of tapers would be to gain greater control of the tapering process. Modifications are currently being made to our fibre drawing tower to allow tailored taper profiles through computer control of the speed at which the fibre is pulled out of the furnace. A similar system is also being constructed for tailored pressure control. Fig. 4.1a shows the change in dispersion when the d/Λ ratio is changed for a constant Λ. The dispersion decreases with little change to the position of the region of zero slope. With greater control over the profile of the pressure transitions, tapers could be fabricated without varying the outer diameter of the fibre, thus simplifying the process. The modifications to the taper fabrication process will allow far greater control over the taper length with greater control over the dispersion profile along the length.

Tapers with ultra-flat dispersion profiles at the output [21] could provide very short output results due to the significant reduction in third order dispersion. Although, these would operate around the 1550 nm telecoms band. Tapered hollow core fibres for ASC have also been demonstrated for high energy soliton compression [90, 91].

Further investigation into SEC in short (<2 mm) lengths of PCF could be done using the method of ref. 85. Particular points would be the use of high power fibre lasers rather than titanium sapphire oscillators as pump sources for pulse generation of a few femtoseconds, or the effects of tapering the short lengths of fibre.

The next chapter presents more work in nonlinear fibre optics. Although it does not directly relate to this chapter soliton dynamics and dispersion engineering again underly the work.

Chapter 5

Supercontinuum generation

5.1 Introduction

The nonlinear mechanisms discussed in chapter 2 give a good understanding of supercontinuum generation, but cannot be said to be complete. In particular, the exact mechanism which defines the "blue" (that is to say the shortest wavelengths, even if they are not actually blue) edge of the supercontinuum cannot clearly be identified. In this chapter we show results which investigate a theory for the defining mechanism for the short wavelength edge of supercontinua, then we show how this theory can be exploited in order to extend the bandwidth of supercontinua to higher frequencies.

5.2 Group index matching

The initial mechanisms for generating wavelengths shorter than the pump wavelength in supercontinuum generation are self phase modulation (strong

for femtosecond pulses), four-wave mixing (when the pump is in the normal dispersion regime) and resonant dispersive wave emission from solitons. It is the latter of these which generates most of the short wavelength radiation in most cases [57]. However for a soliton of given peak power resonant radiation will only be generated around narrow band resonance in the normal dispersion regime and in reasonable proximity to the zero GVD point of the fibre (the bandwidth of the soliton has to overlap with the resonant wavelength). Although many solitons are generated with different peak powers (and hence resonant wavelengths) this cannot account completely for the structure of short wavelength side of the continuum. In particular wavelengths far greater than 600 nm from the zero GVD point can be present. Publications from Nishizawa [92] and Gorbach [93, 94] have explored a concept known as group index matching, proposed here as one of the defining mechanisms for the short wavelength edge of supercontinua. To understand the concept of group index matching we must be familiar with a typical group index curve for a silica fibre, fig. 5.1, which takes the shape of a skewed "U" (when plotted as a function of wavelength). The dispersion in the different regions of the curve, which is related to the derivative of the group index, is also labelled in fig. 5.1. On the short wavelength side of the turning point, corresponding to the zero dispersion wavelength (the minimum of the "U"), the dispersion is normal; on the long wavelength side the dispersion is anomalous. The group index on the short wavelength side of the zero is almost completely defined by the group index of the bulk material and provides little opportunity for modification. However, the long wavelength arm can be strongly modified by waveguide effects. The importance of this will be shown fully later in this chapter.

The idea of group index matching in supercontinua can be understood as follows: part of the initial pulse breaks up into a series of fundamental solitons [53] which then self-frequency shift, propagating up the long wavelength arm of the "U". The initial dispersive radiation on the short wavelength side of the zero GVD point is generated through dispersive wave generation, degenerate FWM and SPM. The dispersive waves initially have a group velocity lower

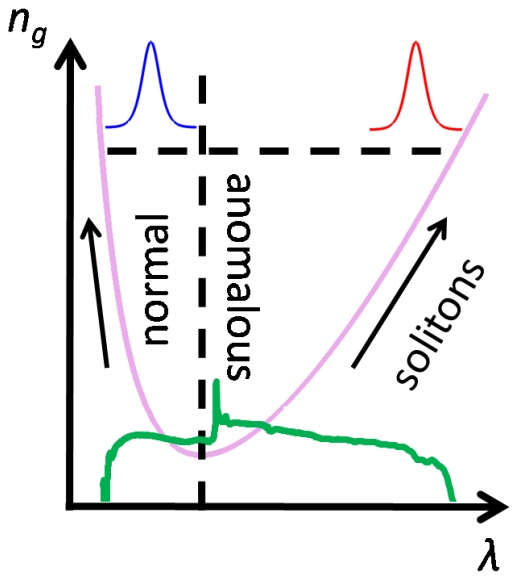

Figure 5.1: A typical group index curve varying with wavelength for a silica fibre. The normal and anomalous dispersion regimes are shown, and schematic representations of a self-frequency-shifting soliton (red) and trapped dispersive radiation (blue) are shown. The span of a supercontinuum pumped in the anomalous dispersion regime is shown in green.

than the solitons; however, as the solitons self frequency shift to longer wavelengths, the group index increases and the solitons continuously slow down so the dispersive radiation catches up. The Kerr-induced refractive index change from the solitons interacts with dispersive radiation propagating with a now similar group index in the short wavelength arm, and shifts the blue radiation to shorter wavelengths in a four-wave mixing process. The soliton continues to slow and again the dispersive radiation catches up and is shifted to shorter wavelengths, and this process is repeated in a cascaded process. This trapped radiation ultimately defines the blue edge, and the solitons define the infrared edge, intimately linking the short and long wavelength edges of supercontinua.

5.3 Femtosecond pumping

In order to provide experimental evidence for the theory of group-index-matched FWM, a highly nonlinear photonic crystal fibre was fabricated from fused silica, shown in fig. 5.2a, using the stack and draw method [5]. The fibre was created to have a zero dispersion wavelength close to 820 nm, the dispersion is plotted in fig. 5.2b. This particular fibre provides a good medium in which to observe supercontinuum generated by a Titanium Sapphire oscillator pump at 800 nm, owing to the proximity of the zero dispersion wavelength to the pump. Our experiment was carried out on a 2 m section of fibre. For femtosecond pulses in a highly nonlinear fibre of 3 μm, core this is many times the nonlinear length which will allow the various stages of the continuum to develop fully.

5.3.1 Experiment

The beam from the Titanium Sapphire oscillator (200 fs pulses at 800 nm wavelength) was aligned with one of the polarisation axes of the fibre by means of a half-wave plate placed before the fibre input. The output continuum was recorded on an optical spectrum analyser (OSA) directly from the fibre using a bare fibre adapter. A 10 cm section of the output end of the fibre was then removed and the output continuum recorded again, and this process was repeated until there was only a 20 cm section of fibre remaining.

5.3.2 Results

The results were then plotted as a function of length, on a logarithmic intensity scale, in order to build up an image of the spectral evolution over the fibre length; this is shown in fig. 5.3. The initial symmetrical spectral broadening

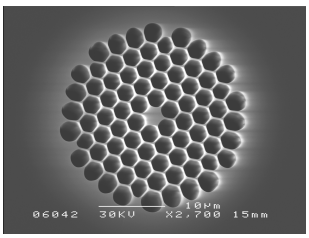

(a)

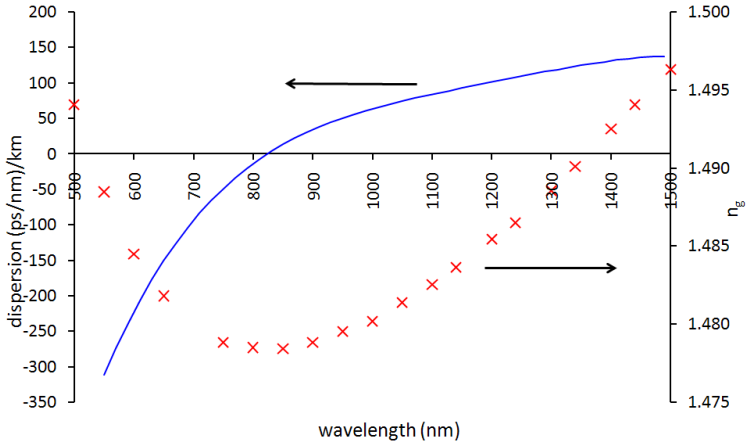

(b)

Figure 5.2: (a) A scanning electron micrograph of the nonlinear optical fibre used for femtosecond continuum generation; the core size is approximately 2.7 μm. (b) Measured group index (crosses) and group velocity dispersion (solid line) profiles for (a).

around the pump (A) is attributed to self phase modulation. The blue edge (B) is then defined by dispersive wave generation from a soliton (Cherenkov radiation) and degenerate four-wave mixing. Spectral broadening on the short wavelength plot as the continuum evolves in this region is minimal. The feature shifting to longer wavelengths (C) from 1.2 m is an ejected fundamental soliton which is a product of soliton fission; at this point the blue edge begins to shift to shorter wavelengths (D). This broadening can be explained in terms of group index matching to the fundamental soliton (C). Fig. 5.4 again shows the evolution of our experimental continuum (fig. 5.4a). Here, modelling by Gorbach [93] has also been included for comparison (fig. 5.4b) along with the group index curve of the fibre (fig. 5.4c). In the modelled case the fibre pa-

rameters and input pulse are set to be the same as in our experiment. The spectral broadening mechanisms identified in the experiment are clear: initial symmetrical broadening, then between 0.2 and 1.2 m no broadening occurs on the short wavelength edge, after which the blue edge begins to shift to shorter wavelengths. The wavelength of the soliton and the wavelength of the shifting dispersive radiation are mapped onto the group index curve for the fibre, and can be seen to be propagating with the same group index in opposite arms of the curve.

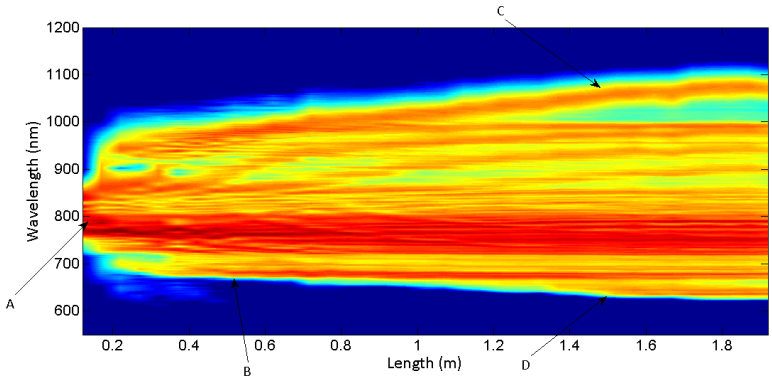

Figure 5.3: Spectral evolution as a function of length for a 3 μm core highly nonlinear fibre pumped at 800 nm. The initial symmetrical broadening around the pump in region A is due to self-phase modulation. The blue edge at B is defined by dispersive wave generation (Cherenkov radiation). A frequency shifting soliton on the long wavelength edge (labelled C) and trapped dispersive radiation on the short wavelength edge (labelled D) can be seen after 1.2 m.

The results of this experiment confirm that group index matching defines the short-wavelength edge of supercontinua. In the next section we show how the cladding structure of PCFs can be modified to take advantage of group index matching and produce continua with bandwidths extending into the blue and ultraviolet regions from pump sources at 1064 nm.

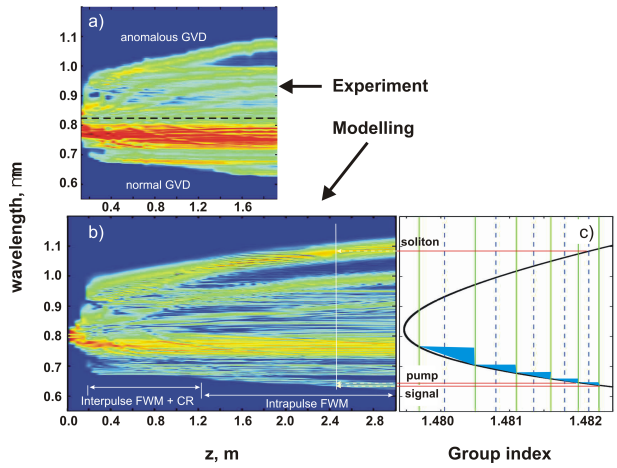

Figure 5.4: (a) Spectral evolution as a function of length as in fig. 5.3. (b) shows simulations with similar parameters to (a), and (c) shows the group index of the fibre aligned to the computed spectrum.

5.4 Nanosecond and picosecond pumping

5.4.1 Introduction

Although supercontinua with wavelengths as short as 400 nm have been generated using a Titanium Sapphire oscillator pumping a small-core highly nonlinear PCF [64], such sources are not practical for day to day laboratory use owing to their bulky nature, high maintenance, lack of portability and high cost. One popular configuration for laboratory supercontinuum systems therefore consists of a section of endlessly single mode (ESM) fibre [6] with a zero dispersion wavelength close to 1064 nm pumped by either a Q-switched Nd:YAG [63] or a commercial high powered fibre laser [81,82] at 1064 nm. The Q-switched sources typically generate continua using sub-nanosecond pulses, providing low-cost bright white light sources for general laboratory use with an average output power of the order of a few tens of milliwatts. The mode-locked high-power fibre laser pumps use pulses of a few picoseconds to generate high power (typically a few watts of average power) continua for applications with more stringent requirements. The bandwidth of these sources, however, seems

to be intrinsically limited on the short wavelength edge to around 450-500 nm, missing the blue frequencies, giving them a "yellow" rather than "white" appearance. The wavelength range immediately below this is of specific interest, as these sources would then incorporate the entire visible spectrum and include a useful spectral band for fluorescence imaging applications [95, 96]. Reported methods of generating deeper blue frequencies include fibre post-processing techniques, fibre tapering and phase matching to higher order modes [68]. Xiong et al. reported on generating a continuum using a small section of fibre taper (1.2 cm) in which, after initial four-wave mixing events had taken place in a conventionally used ESM fibre, the antistokes peak lay close to the zero dispersion wavelength of the taper waist. Kudlinski et al. [70] reported on using longer tapers fabricated on a fibre drawing tower with the zero dispersion wavelength decreasing along the fibre length, allowing phase matching conditions to be satisfied for shorter wavelengths in the fibre.

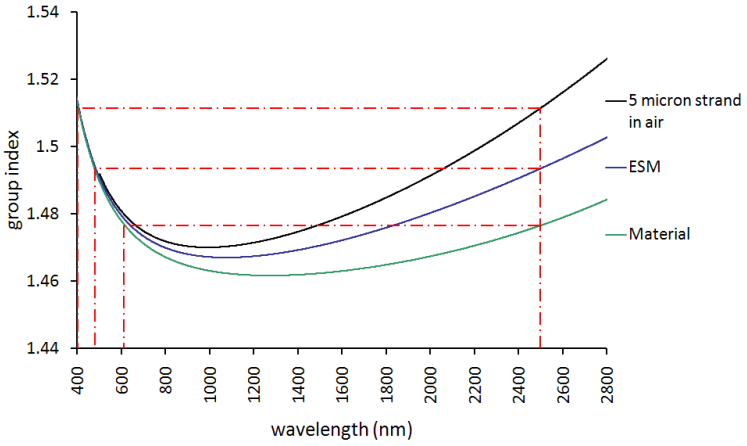

Figure 5.5: Modelled group index curves as a function of wavelength for bulk silica (green), an endlessly single mode fibre with a 5 μm core (blue) and a 5 μm silica strand surrounded by air (black). The red dashed line indicates the intrinsic limit on the long wavelength edge for a frequency shifting soliton at 2500 nm. The group index matched short wavelength edge for each is then shown.

5.4.2 Exploitation of group index matching

The concept of group index matching can be used to enhance the light generated in the blue and ultraviolet regions. The idea behind enhanced blue frequency generation is simple and can be explained using the modelled group index curves in fig. 5.5. The three curves shown are that of: bulk silica (green), a typical ESM fibre (modelled after Saitoh et al. [97]) used for supercontinuum generation (blue) and a silica strand surrounded by air (black). The silica strand is of a similar size to the core region of the ESM fibre, 5 μm. If we look on the short wavelength side of the minima, we can see that all three profiles are similar; they are defined here primarily by the bulk material which leaves little scope for modification. On the long wavelength side, however, clear differences in the steepness of the curves with respect to wavelength can be seen. This is due to increased waveguide effects modifying the bulk curve. The effective index contrast between the cladding and core of the ESM fibre is not as strong as the contrast between the strand and air. This results in the long wavelength arm of the strand being significantly steeper than that of the ESM fibre. Now consider a soliton self-frequency shifting in each of these three cases. In all, the limiting factor for the soliton shift is the rapidly rising material absorption of silica at around 2.5 μm (fig. 5.6 [26]); this is exacerbated in PCFs by the presence of OH^- ions, which have a strong absorption peak around 2.4 μm. This limit is shown in fig. 5.5 by the dashed red line at 2500 nm; the matched wavelengths of similar group index (also joined by horizontal dashed lines) can clearly be seen to shift to shorter wavelengths as the series progresses from bulk material to a strand in air. Thus the intrinsic limit for the generation of deeper blue frequencies is actually governed by the *long wavelength* side of the group index curve. A silica strand in air will therefore allow the generation of deeper blue wavelengths. A simple practical approximation for a silica strand in air is what is known as a high-Δ fibre design, where the cladding region incorporates a high air-filling fraction, as shown in fig. 5.7(b). This design is common for smaller 'highly nonlinear' PCFs [71], which typically have a core size between 1 and 3 μm, but has not previously

been exploited on a larger scale for supercontinuum applications.

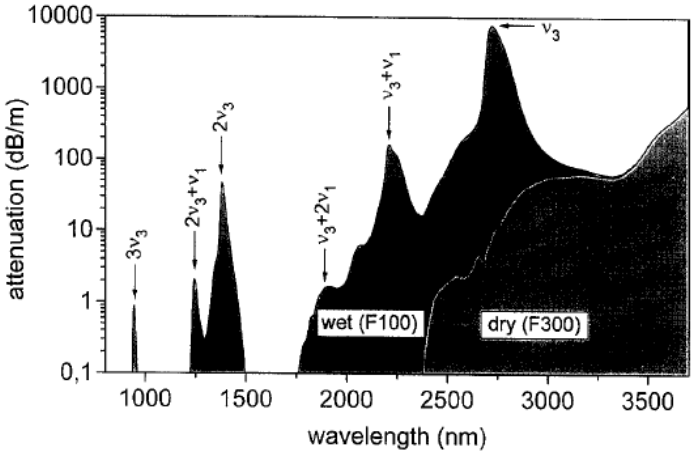

Figure 5.6: Bulk attenuation spectra for wet (high OH content, F100) and dry (low OH content, F300) synthetic silica. The labels refer to the specific overtones which make up the peaks, where ν_3 and ν_1 refer to the fundamental OH vibration and SiO_4 tetrahedron vibration respectively. Reproduced from ref. 26.

5.4.3 Experiment

A large-core high-Δ fibre was fabricated ($d/\Lambda = 0.77$ and $\Lambda = 3.7$, fig. 5.7) from fused silica (Heraeus F300) using the stack and draw method [1]. An identical length of ESM fibre ($d/\Lambda = 0.43$ and $\Lambda = 3.0$, fig. 5.7) was used for comparison. The core sizes of both fibres were 4.7 μm. Sub-ns (600 ps) pulses from a microchip laser at 1064 nm, $\approx$ 60 mW average output power and 7 kHz repetition rate, were launched into 10 m sections of each fibre. The input power was varied by means of a neutral density filter placed before the fibre input. We measured the output power using a thermal power meter placed at the fibre output for direct comparison between the two fibres. The visible component of the dispersed output spectra of both fibres under identical pump conditions, as recorded by a digital camera, can be seen in fig. 5.8. The high-Δ fibre can be seen glowing white with blue and violet frequencies in

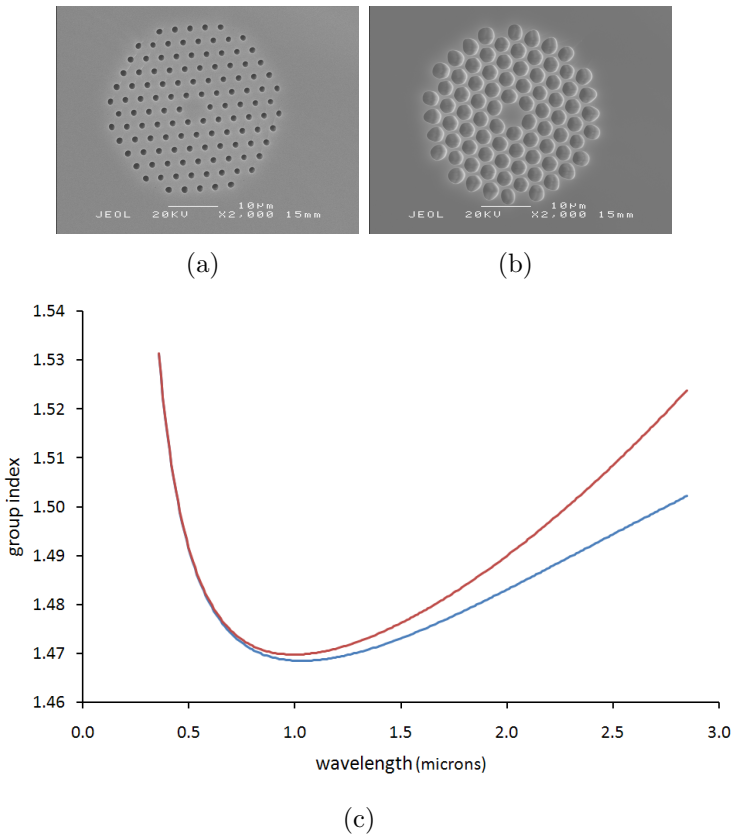

Figure 5.7: Scanning electron micrographs of (a) the endlessly single-mode fibre ($d/\Lambda = 0.43$ and $\Lambda = 3.0$) and (b) the high-Δ fibre ($d/\Lambda = 0.77$ and $\Lambda = 3.7$). (c) Shows the corresponding modelled group index curves for (a) blue and (b) red.

its spectrum. The short wavelength output (350-1750 nm) was collected by a multimode fibre and recorded on an optical spectrum analyser (Ando AO-63158), and the long wavelength edge (1100-2550 nm) of the continuum was collected by a short straight length of single mode fibre and recorded on a near infrared spectrometer (Ocean Optics NIR-256). The pump peaks were filtered out using a long pass filter (cut-off wavelength 1600 nm) to prevent multi-order interference in the measurement. The complete spectrum for the high-Δ fibre at the highest recorded output power can be seen in fig. 5.8 extending from 400 to 2500 nm.

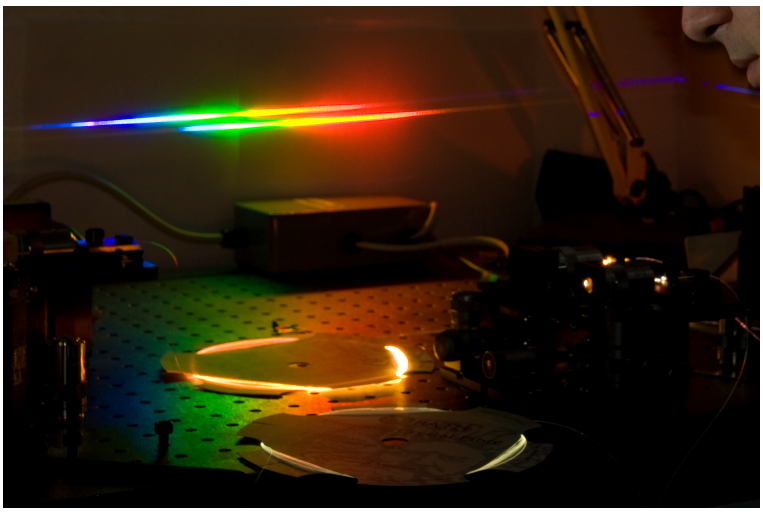

(a)

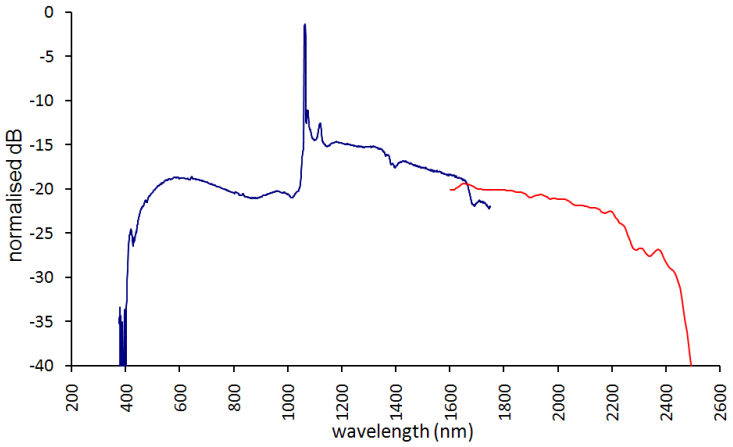

(b)

Figure 5.8: (a) A digital photograph showing a comparison of our two tested fibres pumped by sub-ns 1064 nm microchip lasers. The endlessly single mode fibre is glowing yellow and its dispersed output spectrum is the lower of the two; the dimmer white fibre is our high-Δ fibre and its dispersed output spectrum can be seen at the top clearly including blue and violet frequencies. (b) Shows the full output spectrum from our high-Δ fibre. The short wavelengths were recorded on an OSA (blue) and the long wavelengths were recorded on a near infrared spectrometer (red).

Spectra were recorded for four different output powers using each fibre. The short and long wavelength edges were defined by identifying a point at a fixed

value (either 10, 15 or 20 dB below a feature which appeared in all the spectra for either the long or short wavelength edges). The edges were then overlaid onto the two modelled group index curves as shown in fig. 5.7(c), and are shown in fig. 5.9. The points at either side of the spectrum for different powers are joined by straight lines. The agreement is good; that is, the lines joining the short and long wavelength edges are almost horizontal on the plot. This gives strong support to the concept that group index matching is also the limiting factor in ultraviolet continuum generation for sub-nanosecond pulses.

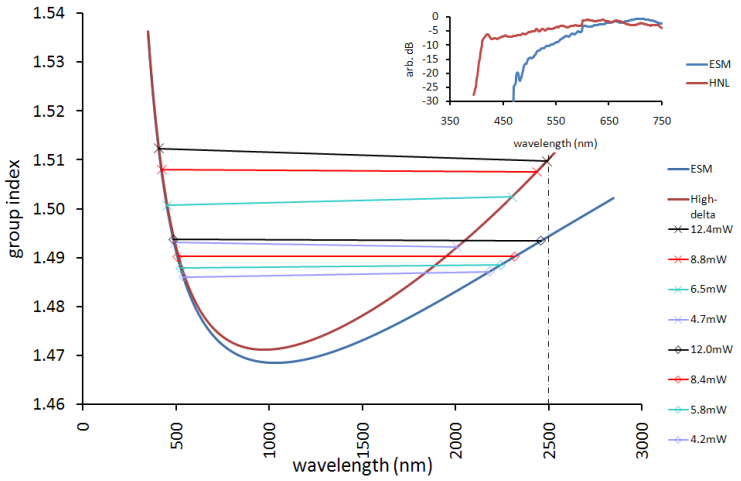

Figure 5.9: Modelled group index curves for the two tested fibres, overlaid onto them are the edges of the continua for different output powers. Corresponding short and long wavelength edges are joined together. The insert shows the blue edges of both continua on full power.

5.4.4 Optimisation

The optimisation of the high-Δ fibre to generate the shortest possible wavelengths without detrimental effects to other properties of the supercontinuum is important. Modelling of different fibres with the same d/Λ ratio but smaller Λ (and hence core size) is shown in fig. 5.10a. This shows that simply decreasing the fibre size causes the infrared arm of the group index curve to steepen, which in turn would lead to group index matching to a deeper blue. Two fur-

ther smaller fibres were drawn (we refer to them by their core sizes, see section 1.4: 4.4 μm and 4.2 μm) in addition to the high-Δ fibre used in the previous experiment. All had the same d/Λ. The modelled group index curves for these fibres are shown in fig. 5.10a. The infrared edge can be seen to steepen as the pitch becomes smaller, indicating that shorter wavelength generation should be possible in these fibres. In order to test this, the fibres were then pumped with the same sub-nanosecond source as the earlier experiments, and the short wavelength edge again recorded on an OSA. The series is plotted in fig. 5.10b.

The shapes of the individual spectra do indeed stretch to shorter wavelengths for the smaller cores. However, there is approximately a 5 dB decrease in the visible spectrum for the successively smaller cores where no decrease was observed on the long wavelength side of the pump. The primary mechanism for supercontinuum generation on the long wavelength side of the pump is Raman-shifting solitons, which are largely unaffected by the proximity of the pump to the zero dispersion wavelength of the fibre. However, on the short wavelength side, new frequencies are initially generated by other processes such as four wave mixing and dispersive wave generation, before being shifted by group index matching. These processes require the pump to be in close proximity to the zero dispersion point of the fibre. As the fibre pitch is changed in order to steepen the infrared edge, the zero dispersion wavelength is also further shifted away from the pump, reducing the intensity of the dispersive radiation initially generated which is then blue shifted. Similar experiments were carried out on the same fibres using a fibre laser (Fianium Femtopower 1060-1μJ-pp, 0.5 kHz repetition rate) emitting 7 ps pulses at 1064 μm as a pump. The results are shown in fig. 5.10(c). In this case, the spectra did not show any decrease in the visible intensity between the successive fibres. A possible explanation for this is that the 7 ps pulses are inherently broader and experience more SPM and dispersive wave generation than the sub-ns pulses. The increased SPM shifts more radiation closer to the zero dispersion wavelength.

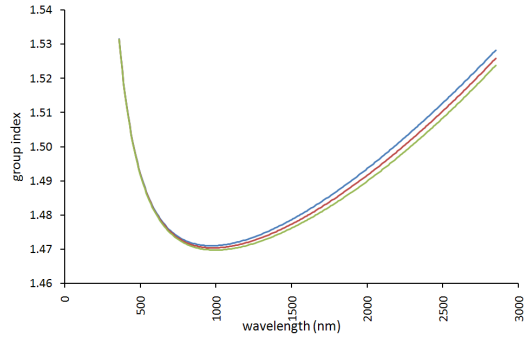

(a)

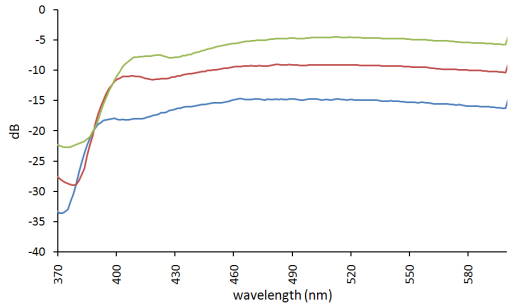

(b)

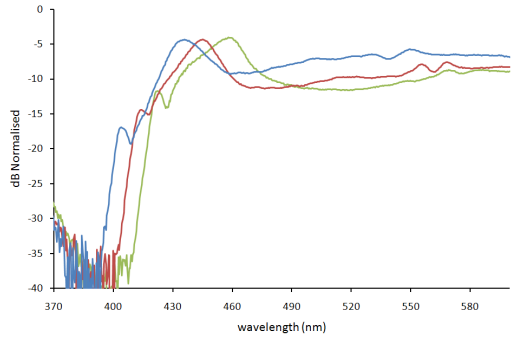

(c)

Figure 5.10: (a) Shows the modelled group index curves for a series of progressively smaller fibres with the same d/Λ ratio; core size=4.7, 4.4 and 4.2 μm, shown in green, red and blue respectively. (b) shows the short wavelength edge for the same fibre series with sub-nanosecond pumping; the colouring is the same as in (a). (c) shows the shortwavelength edge of the same fibre series under pumping from a commercial high-power picosecond fibre laser. The spectra in (c) have been normalised to the peak intensity; however, those in (b) have been left un-normalised in order to show the observed 5 dB decrease between smaller fibres.

5.4.5 Computational optimisation

Further modelling of high-Δ fibres was carried out. First we discuss the effect of shifting the zero dispersion wavelength from ≈980 nm to the pump wavelength by making the fibre larger. Fig. 5.11a shows four group index curves: the ESM and high-Δ fibre used for our initial comparison, and two larger high-Δ fibres. The larger fibres both have $d/\Lambda = 0.84$ with Λ =4.64 μm and 5.64 μm respectivly. The zero dispersion wavelength of the largest fibre has been shifted to approximately 1060 nm, some 80 nm longer than our original fibre. Making the fibre larger, however, has also modified the long wavelength arm of the group index curve. The group index at 2500 nm is now comparable that of the ESM fibre, indicating that no advantage in terms of blue frequency generation would be gained if the zero dispersion wavelength were at the pump wavelength. The mismatch between the zero dispersion wavelength and the pump is therefore critical in generating additional blue frequencies through this fibre design.

In the second case shown in fig. 5.11b, silica strands of progressively smaller sizes are plotted until the second zero dispersion wavelength (shown as a turning point in the group index curve) comes down to 2500 nm. At this point the dispersion changes from anomalous to normal with increasing wavelength, providing a limit to soliton propagation. If this is shifted below the absorption band around 2500 nm, it will become the limiting factor in group index matching. Therefore the strand where the second turning point is at the absorption will provide the steepest long wavelength edge without prohibiting soliton propagation over the transmission window of silica. It can clearly be seen that the 2 μm strand provides this case, and indicates that a short wavelength edge of around 300 nm should be achievable. This strand has a zero between 700 and 800 nm, so would be ideal for Titanium Sapphire laser systems. This core size is similar to that of the fibre used in the first reported supercontinuum generation by Ranka [64]. The generated continuum in this publication stretched from 400 nm to 1500 nm which matches closely in group

index on our curve. The mismatch in wavelength with our theoretical minimum implies that the full extent of the possible ultraviolet continuum that could be generated in this fibre was not exploited.

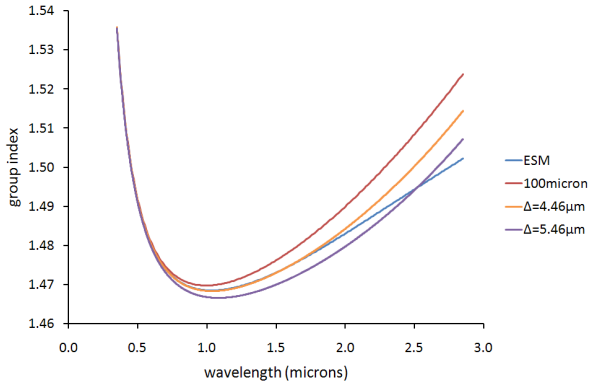

(a)

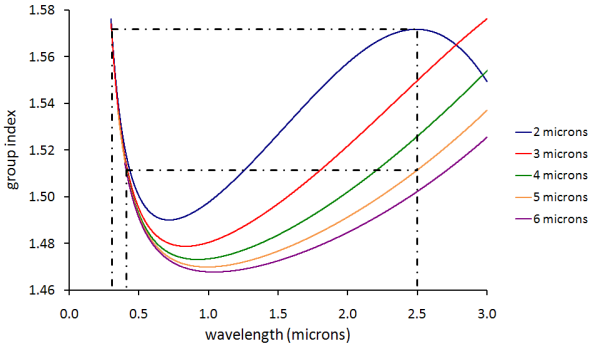

(b)

Figure 5.11: (a) Shows modelled group index curves for the two measured fibres and two larger high-Δ fibres, Λ =4.46 μm (orange) and Λ =5.46 μm (purple). In both cases $d/\Lambda = 0.836$. (b) Shows a series of modelled group index curves for silica strands in air. The dashed lines indicate which the theoretical extent of group index matched continua for the 2 μm and 5 μm strands, limited at 2500 nm on the long wavelength edge.

5.5 Ultraviolet grade silica

Ultraviolet grade silica is fused silica that has not undergone purification processes involving Cl^- ions (which are used to remove troublesome OH^- ions). Chlorine has strong absorption bands in the ultraviolet part of the spectrum, so ultraviolet grade silica has lower losses in the ultraviolet band, which could potentially prove useful for ultraviolet-enhanced supercontinuum generation. A fibre series with similar core sizes to those compared in the previous section was fabricated using ultraviolet grade silica (Heraeus F100 fig. 5.6) as shown in fig. 5.12(a). The fibres were pumped with the same 7 ps source reported in the previous section and the resulting spectra recorded on an OSA, fig. 5.12(b).

Although shifting to shorter wavelengths for progressively smaller cores can still be observed, the edges are approximately 50 nm higher than our F300 fibres, and there are also large absorption peaks in the spectra. The inclusion of more OH^- ions gives rise to strong water absorption peaks, which are particularly noticeable around 1340 nm where the loss in this region nearly exceeds the gain from supercontinuum generation. After this point there is a 10 dB decrease in the intensity of the continuum. This is most likely a result of the Raman shifting solitons losing energy as they pass through the absorption peak. The strong OH^- absorption band around 2.4 μm, shown in fig. 5.6, is dramatically larger. This limits how far a frequency shifting soliton can progress, in turn, through group index matching. This will be the most likely limitation on the short wavelength edge.

5.6 Conclusions

Group index matching has been investigated experimentally to confirm that it is the limiting factor of the short wavelength edge of supercontinua. With this additional understanding in supercontinuum dynamics we redesigned the

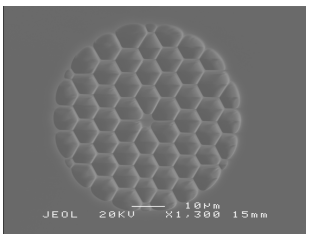

(a)

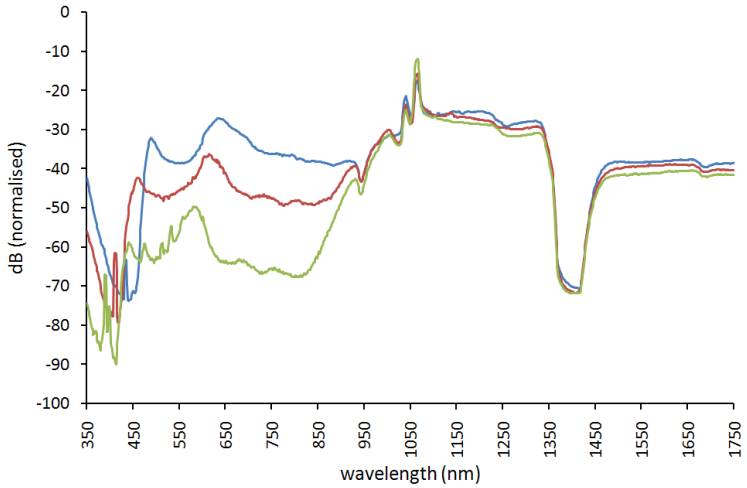

(b)

Figure 5.12: (a) Shows a scanning electron micrograph of an ultraviolet grade silica high-Δ fibre. (b) Shows the short wavelength spectra recorded on an OSA for the ultraviolet fibre series. Although shifting to shorter wavelengths for smaller cores can still be observed, the recorded edges are not as short as fused silica, and large water absorption peaks can also be seen.

cladding structure of PCFs, used to generate continua from 1064 nm pump sources, and exploited group index matching to generate continua incorporating the entire visible spectrum, <400 nm. Ultraviolet grade silica has been explored as a possibility to enhance further in the visible-ultraviolet; however, the presence of greater amounts of OH^- ions has proved too detrimental to the supercontinuum generation process to warrant further investigation.

Chapter 6

Conclusions and the future

In this thesis we have explored linear and nonlinear properties of PCFs fabricating new fibres with improved designs. Several new designs have been modelled, fabricated and characterised for different applications.

In chapter 3 we reported on an all-solid photonic bandgap fibre with restructured cladding matrix. The replacement of high-index rods with thin rings reorganises the cladding modes, suppressing those which couple strongly to the fundamental core mode when the fibre is bent. We have experimentally verified that suppression of these modes reduces losses when the fibre is bend by comparing the performance of our fibre to a similar (in core size, pitch etc. rod fibre. The method of fabricating the cladding structure, by stacking the unit cell and drawing it to canes demonstrates a method of creating novel cladding structures.

In chapter 4 we demonstrated the use of dispersion-decreasing PCF tapers in order to compress optical solitons. A maximum compression factor of 15 at 1064 nm was achieved in two tapers, with pulses as short as 43 fs generated in one of the tapers. Although these tapers were both initially fabricated for compression via adiabatic soliton compression, the soliton length for the input

pulse was too short in one of the tapers for adiabatic soliton compression to be acting alone. The total compression was attributed to the combined contributions of adiabatic soliton compression and soliton effect compression. The compression in these tapers is limited by the extent of the anomalous dispersion region. Better control over the fabrication could lead to shorter pulses.

In chapter 5 we demonstrated experimentally that group index matching is the responsible effect for defining the short wavelength edge of supercontinua. We then showed how modifying the cladding structure of fibres typically used for supercontinuum generation with 1064 nm pump sources can extend the bandwidth of supercontinuum sources <400 nm, some 50 nm deeper than previously reported in uniform fibres. This result is not only important in the field of optics, but has broadened the applications of supercontinuum sources in medical imaging. In particular, an important line for cytology lies at 405 nm and supercontinuum sources based on our improved design now achieve this wavelength and are being sold commercially.

Although my work has advanced the field, it still remains fertile. Medical imaging techniques still require supercontinuum sources with shorter wavelengths and commercial fibre laser companies are interested in solitonic pulse compression to deliver high-power, ultrashort, bandwidth-limited pulses. In these cases my work has taken the first step, but there remains plenty still to do.

Appendix A

List of acronyms

TIR	Total internal reflection
PCF	Photonic crystal fibre
PBGF	Photonic bandgap fibre
HC-PCF	Hollow core photonic crystal fibre
AS-PCF	All solid photonic crystal fibre
GVD	Group velocity dispersion
MI	Modulation instability
FWM	Four wave mixing
SPM	Self phase modulation
XPM	Cross phase modulation
SRS	Stimulated Raman scattering
SBS	Stimulated Brillouin scattering
SEC	Soliton effect compression
ASC	Adiabatic soliton compression
ARROW	Anti-resonant reflecting optical waveguide
DOS	Density of states
OSA	Optical spectrum analyser

Appendix B

Publications list

B.1 Journal publications

J. M. Stone, G. J. Pearce, F. Luan, T. A. Birks, J. C. Knight, A. K. George, and D. M. Bird. An improved photonic bandgap fiber based on an array of rings. *Opt. Express*, 14(13):6291–6296, 2006.

A. V. Gorbach, D. V. Skryabin, J. M. Stone, and J. C. Knight. Four-wave mixing of solitons with radiation and quasi-nondispersive wave packets at the short-wavelength edge of a supercontinuum. *Opt. Express*, 14(21):9854–9863, 2006.

Ł. W. Kornaszewski, N. Gayraud, J. M. Stone, W. N. MacPherson, A. K. George, J. C. Knight, D. P. Hand, and D. T. Reid. Mid-infrared methane detection in a photonic bandgap fiber using a broadband optical parametric oscillator. *Opt. Express*, 15(18):11219–11224, 2007.

J. C. Travers, J. M. Stone, A. B. Rulkov, B. A. Cumberland, A. K. George,

S. V. Popov, J. C. Knight, and J. R. Taylor. Optical pulse compression in dispersion decreasing photonic crystal fiber. *Opt. Express*, 15(20):13203–13211, 2007.

J. M. Stone and J. C. Knight. Visibly "white" light generation in uniform-photonic crystal fiber using a microchip laser. *Opt. Express*, 16(4):2670–2675, 2008.

N. Gayraud, Ł. W. Kornaszewski, J. M. Stone, J. C. Knight, D. T. Reid, D. P. Hand, and W. N. MacPherson. Mid-infrared gas sensing using a photonic bandgap fiber. *Appl. Opt.*, 47(9):1269–1277, 2008.

Yan-Wei Tzeng, Yen-Yin Lin, Chen-Han Huang, Jian-Ming Liu, Hsiang-Chen Chui, Hsiang-Lin Liu, J. M. Stone, J. C. Knight and Shi-Wei Chu. Broadband tunable optical parametric amplification from a single 50 MHz ultrafast fiber laser. *Opt. Express*, 17(9):7304–7309, 2009.

B.2 Conference publications

J. M. Stone, F. Luan, G. J. Pearce, T. A. Birks, J. C. Knight and D. M. Bird. Photonic bandgap fibre based on a 2-d array of cladding rings. In *Photon 06*. Institute of Physics, 2006.

G. J. Pearce, J. M. Stone, F. Luan, T. A. Birks, J. C. Knight and D. M. Bird. Bend loss in bandgap-guiding photonic crystal fibre. In *Photon 06*. Institute of Physics, 2006.

J. D. Shephard, N. Gayraud, W. N. MacPherson, R. R. Maier, J. D. Jones, D. P. Hand, J. M. Stone, A. K. George, J. C. Knight and M. Mohebbi. Silica

based air-core photonic crystal fibres for mid IR gas sensing applications. In *Photon 06*. Institute of Physics, 2006.

N. Gayraud, W. N. MacPherson, J. D. Shephard, R. R. Maier, D. P. Hand, J. D. Jones, J. M. Stone, A. K. George, and J. C. Knight. Mid infra-red gas sensing using a hollow-core photonic bandgap fibre. In *Optical Fiber Sensors*, page ThA5. Optical Society of America, 2006.

Ł W. Kornaszewski, N. Gayraud, W. N. MacPherson, D. P. Hand, D. T. Reid, J. M. Stone, A. K. George, and J. C. Knight. Mid-infrared methane sensing using an optical parametric oscillator and a photonic bandgap fiber as a gas cell. In *Conference on Lasers and Electro-Optics/Quantum Electronics and Laser Science Conference and Photonic Applications Systems Technologies*, page CThO3. Optical Society of America, 2007.

J. M. Stone, A. K. George, J. C. Knight, J. C. Travers, B. A. Cumberland, A. B. Rulkov, S. V. Popov, and J. R. Taylor. Pulse compression at 1.06μm in dispersion decreasing photonic crystal fibers. In *Nonlinear Photonics*, page NThB2. Optical Society of America, 2007.

J. C. Travers, B. A. Cumberland, A. B. Rulkov, S. V. Popov, J. R. Taylor, J. M. Stone, A. K. George, and J. C. Knight. Pulse compression in dispersion decreasing photonic crystal fiber. In *Conference on Lasers and Electro-Optics/Quantum Electronics and Laser Science Conference and Photonic Applications Systems Technologies*, page CFK1. Optical Society of America, 2007.

N. Gayraud, Ł. W. Kornaszewski, D. T. Reid, W. N. MacPherson, D. P. Hand, J. M. Stone, A. K. George, and J. C. Knight. Mid-infrared methane sensing using a silica photonic bandgap fiber. In *CLEO/Europe and IQEC 2007 Conference Digest*, page $CH3_2.Optical Society of America$, 2007.

J. M. Stone, J. C. Knight, and J. Clowes. Visibly "white" light generation in uniform photonic crystal fiber using a microchip laser. In *Conference on Lasers and Electro-Optics/Quantum Electronics and Laser Science Conference and Photonic Applications Systems Technologies*, page CMT5. Optical Society of America, 2008.

J. C. Knight and J. M. Stone. Extending fiber-based supercontinuum generation to shorter wavelengths (*Invited paper*). In *Photonics West*, SPIE, 2009.

D. T. Reid, Ł. W. Kornaszewski, T. P. Mueller, N. Gayraud, W. N. MacPherson, D. P. Hand, J. M. Stone and J. C. Knight. Ultrafast parametric oscillators for spectroscopy. In *Photonics West*, SPIE, 2009.

References

[1] J. C. Knight. Photonic crystal fibres. *Nature*, 424:847–851, 2003.

[2] P. St. J. Russell. Photonic crystal fibres. *Science*, 299:358–362, 2003.

[3] A. W. Snyder and J. D. Love. *Optical Waveguide Theory*. Kluwer Academic Pub, 1983.

[4] O. V. Butov, K. M. Golant, A. L. Tomashuk, M. J. N. van Stralen, and A. H. E. Breuls. Refractive index dispersion of doped silica for fiber optics. *Optics Communications*, 213(4-6):301–308, 2002.

[5] J. C. Knight, T. A. Birks, P. St. J. Russell, and D. M. Atkin. All-silica single-mode optical fiber with photonic crystal cladding. *Opt. Letters*, 21(19):1547–1549, 1996.

[6] T. A. Birks, J. C. Knight, and P. St. J. Russell. Endlessly single-mode photonic crystal fiber. *Opt. Letters*, 22(13):961–963, 1997.

[7] J. C. Knight, T. A. Birks, R. F. Cregan, P. St. J. Russell, and P. D. de Sandro. Large mode area photonic crystal fibre. *Electronics Letters*, 34(13):1347–1348, 1998.

[8] R. F. Cregan, B. J. Mangan, J. C. Knight, T. A. Birks, P. S. J. Russell, P. J. Roberts, and D. C. Allan. Single-Mode Photonic Band Gap Guidance of Light in Air. *Science*, 285(5433):1537, 1999.

[9] R. Amezcua-Correa, F. Gèrôme, S. G. Leon-Saval, N. G. R. Broderick, T. A. Birks, and J. C. Knight. Control of surface modes in low losshollow-core photonic bandgap fibers. *Opt. Express*, 16(2):1142–1149, 2008.

[10] F. Benabid, J. C. Knight, G. Antonopoulos, and P. St. J. Russell. Stimulated Raman Scattering in Hydrogen-Filled Hollow-Core Photonic Crystal Fiber. *Science*, 298(5592):399–402, 2002.

[11] F. Couny, F. Benabid, and P. S. Light. Large-pitch kagome-structured hollow-core photonic crystal fiber. *Opt. Letters*, 31(24):3574–3576, 2006.

[12] G. J. Pearce, G. S. Wiederhecker, C. G. Poulton, S. Burger, and P. St. J. Russell. Models for guidance in kagome-structured hollow-core photonic crystal fibres. *Opt. Express*, 15(20):12680–12685, 2007.

[13] P. S. Light, F. Benabid, F. Couny, M. Maric, and A. N. Luiten. Electromagnetically induced transparency in rb-filled coated hollow-core photonic crystal fiber. *Opt. Letters*, 32(10):1323–1325, 2007.

[14] Ł. W. Kornaszewski, N. Gayraud, J. M. Stone, W. N. MacPherson, A. K. George, J. C. Knight, D. P. Hand, and D. T. Reid. Mid-infrared methane detection in a photonic bandgap fiber using a broadband optical parametric oscillator. *Opt. Express*, 15(18):11219–11224, 2007.

[15] G. Bouwmans, L. Bigot, Y. Quiquempois, F. Lopez, L. Provino, and M. Douay. Fabrication and characterization of an all-solid 2d photonic bandgap fiber with a low-loss region (< 20 db/km) around 1550 nm. *Opt. Express*, 13(21):8452–8459, 2005.

[16] F. Luan, A. K. George, T. D. Hedley, G. J. Pearce, D. M. Bird, J. C. Knight, and P. St. J. Russell. All-solid photonic bandgap fiber. *Opt. Letters*, 29(20):2369–2371, 2004.

[17] J. C. Maxwell. A Dynamical Theory of the Electromagnetic Field. *Roy . Soc. Trans.*, CLV:459, 1865.

[18] A. Yariv. *Optical Electronics in Modern Communications*. Bibliographical Society, 1997.

[19] R. Lundin. Dispersion flattening in a W fiber. *Applied Optics*, 33(6/20), 1994.

[20] T. A. Birks, W. J. Wadsworth, and P. St. J. Russell. Supercontinuum generation in tapered fibers. *Opt. Letters*, 25(19):1415–1417, 2000.

[21] W. H. Reeves, J. C. Knight, P. St. J. Russell, and P. J. Roberts. Demonstration of ultra-flattened dispersion in photonic crystal fibers. *Opt. Express*, 10(14):609–613, 2002.

[22] J. C. Knight, J. Arriaga, T. A. Birks, A. Ortigosa-Blanch, W. J. Wadsworth, and P. St. J. Russell. Anomalous dispersion in photonic crystal fiber. *Photonics Technology Letters, IEEE*, 12(7):807–809, 2000.

[23] J. C. Travers, J. M. Stone, A. B. Rulkov, B. A. Cumberland, A. K. George, S. V. Popov, J. C. Knight, and J. R. Taylor. Optical pulse compression in dispersion decreasing photonic crystal fiber. *Opt. Express*, 15(20):13203–13211, 2007.

[24] J. Schroeder. Light scattering in glass. *in Treatise on Materials Science and Technology*, 12, 1977.

[25] www.heraeus-quarzglas.com.

[26] O. Humbach, H. Fabian, U. Grzesik, U. Haken, and W. Heitmann. Analysis of OH absorption bands in synthetic silica. *Journal of non-crystalline solids*, 203:19–26, 1996.

[27] P. J. Roberts, F. Couny, H. Sabert, B. J. Mangan, D. Williams, L. Farr, M. Mason, A. Tomlinson, T. A. Birks, J. C. Knight, and P. St. J. Russell. Ultimate low loss of hollow-core photonic crystal fibres. *Opt. Express*, 13(1):236–244, 2005.

[28] P. J. Roberts, F. Couny, H. Sabert, B. J. Mangan, T. A. Birks, J. C. Knight, and P. St. J. Russell. Loss in solid-core photonic crystal fibers due to interface roughness scattering. *Opt. Express*, 13(20):7779–7793, 2005.

[29] T. P. White, R. C. McPhedran, C. Martijnde Sterke, N. M. Litchinitser, and B. J. Eggleton. Resonance and scattering in microstructured optical fibers. *Opt. Letters*, 27(22):1977–1979, 2002.

[30] N. Litchinitser, S. Dunn, B. Usner, B. Eggleton, T. White, R. McPhedran, and C. de Sterke. Resonances in microstructured optical waveguides. *Opt. Express*, 11(10):1243–1251, 2003.

[31] M. A. Duguay, Y. Kokubun, T. L. Koch, and Loren Pfeiffer. Antiresonant reflecting optical waveguides in sio[sub 2]-si multilayer structures. *Applied Physics Letters*, 49(1):13–15, 1986.

[32] T. Baba and Y. Kokubun. Dispersion and radiation loss characteristics of antiresonantreflecting optical waveguides-numerical results and analyticalexpressions. *QJournal of quantum Electronics, IEEE*, 28(7):1689–1700, 1992.

[33] A. Argyros, T. Birks, S. Leon-Saval, C. M. Cordeiro, F. Luan, and P. St. J. Russell. Photonic bandgap with an index step of one percent. *Opt. Express*, 13(1):309–314, 2005.

[34] E. Hecht. *Hecht Optics*. Addison-Wesley, 1998.

[35] J. M. Stone, G. J. Pearce, F. Luan, T. A. Birks, J. C. Knight, A. K. George, and D. M. Bird. An improved photonic bandgap fiber based on an array of rings. *Opt. Express*, 14(13):6291–6296, 2006.

[36] A. Wang, G. J. Pearce, F. Luan, D. M. Bird, T. A. Birks, and J. C. Knight. All solid photonic bandgap fiber based on an array of oriented rectangular high index rods. *Opt. Express*, 14(22):10844–10850, 2006.

[37] R. B. Dyott. Some memories of the early years with optical fibres at the British Post Office: a personal account. *IEE Proceedings J Optoelectronics [see also IEE Proceedings-Optoelectronics]*, 133(3):199–201, 1986.

[38] C. Xiong and W. J. Wadsworth. Polarized supercontinuum in birefringent photonic crystal fibre pumped at 1064 nm and application to tuneable visible/uv generation. *Opt. Express*, 16(4):2438–2445, 2008.

[39] K. M. Kiang, K. Frampton, T. M. Monro, R. Moore, J. Tucknott, D. W. Hewak, D. J. Richardson, and H. N. Rutt. Extruded singlemode non-silica glass holey optical fibres. *Electronics Letters*, 38(12):546–547, 2002.

[40] V. V. Ravi Kanth Kumar, A. K. George, J. C. Knight, and P. St. J. Russell. Tellurite photonic crystal fiber. *Opt. Express*, 11(20):2641–2645, 2003.

[41] V. V. Ravi Kanth Kumar, A. K. George, W. H. Reeves, J. C. Knight, P. St. J. Russell, F. Omenetto, and A. Taylor. Extruded soft glass photonic crystal fiber for ultrabroad supercontinuum generation. *Opt. Express*, 10(25):1520–1525, 2002.

[42] G. P. Agrawal. *Nonlinear fiber optics*. Academic press, 2007.

[43] G. P. Agrawal. *Applications of nonlinear fiber optics*. Academic Press, 2001.

[44] K. Nagayama, T. Saito, M. Kakui, K. Kawasaki, M. Matsui, H. Takamizawa, H. Miyaki, Y. Ogo, and Y. Chigusa. Ultra Low Loss (0.151 dB/km) Pure Silica Core Fiber and Extension of Transmission Distance. *IEIC Technical Report (Institute of Electronics, Information and Communication Engineers)*, 102(135):1–6, 2002.

[45] B. A. Cumberland, J. C. Travers, S. V. Popov, and J. R. Taylor. 29 w high power cw supercontinuum source. *Opt. Express*, 16(8):5954–5962, 2008.

[46] http://www.rp-photonics.com/encyclopedia.html.

[47] F. M. Mitschke and L. F. Mollenauer. Discovery of the soliton self-frequency shift. *Opt. Letters*, 11(10):659–661, 1986.

[48] J. P. Gordon. Theory of the soliton self-frequency shift. *Opt. Letters*, 11(10):662–664, 1986.

[49] F. Benabid, J. C. Knight, G. Antonopoulos, and P. St. J. Russell. Stimulated Raman Scattering in Hydrogen-Filled Hollow-Core Photonic Crystal Fiber. *Science*, 298(5592):399–402, 2002.

[50] F. Couny, F. Benabid, P. J. Roberts, P. S. Light, and M. G. Raymer. Generation and Photonic Guidance of Multi-Octave Optical-Frequency Combs. *Science*, 318(5853):1118, 2007.

[51] Y. S. Kivshar and G. P. Agrawal. *Optical solitons*. Academic press, 2007.

[52] L. F. Mollenauer, R. H. Stolen, and J. P. Gordon. Experimental observation of picosecond pulse narrowing and solitons in optical fibers. *Phys. Rev. Lett.*, 45(13):1095–1098, Sep 1980.

[53] Y. Kodama and A. Hasegawa. Nonlinear pulse propagation in a monomode dielectric guide. *Journal of Quantum Electronics, IEEE*, 23(5):510–524, May 1987.

[54] A. K. Atieh, P. Myslinski, J. Chrostowski, and P. Galko. Measuring the Raman Time Constant (T_R) for Soliton Pulses in Standard Single-Mode Fiber. *Journal of Lightwave Technology*, 17(2):216, 1999.

[55] R. H. Hardin and F. D. Tappert. Applications of the split-step Fourier method to the numerical solution of nonlinear and variable coefficient wave equations. *Siam Rev*, 15(423):0–021, 1973.

[56] R. A. Fisher and W. Bischel. The role of linear dispersion in plane-wave self-phase modulation. *Applied Physics Letters*, 23:661, 1973.

[57] J. M. Dudley, G. Genty, and S. Coen. Supercontinuum generation in photonic crystal fiber. *Reviews of Modern Physics*, 78(4):1135–1184, 2006.

[58] N. Akhmediev and M. Karlsson. Cherenkov radiation emitted by solitons in optical fibers. *Phys. Rev. A*, 51(3):2602–2607, Mar 1995.

[59] D. V. Skryabin and A. V. Yulin. Theory of generation of new frequencies by mixing of solitons and dispersive waves in optical fibers. *Phys. Rev. E*, 72(1):016619, Jul 2005.

[60] P. K. A. Wai, C. R. Menyuk, Y. C. Lee, and H. H. Chen. Nonlinear pulse propagation in the neighborhood of the zero-dispersion wavelength of monomode optical fibers. *Opt. Letters*, 11(7):464–466, 1986.

[61] F Shimizu. Frequency broadening in liquids by a short light pulse. *Phys. Rev. Lett.*, 19(19):1097–1100, Nov 1967.

[62] R. R. Alfano and S. L. Shapiro. Emission in the region 4000 to 7000 å via four-photon coupling in glass. *Phys. Rev. Lett.*, 24(11):584–587, Mar 1970.

[63] W. J. Wadsworth, N. Joly, J. C. Knight, T. A. Birks, F. Biancalana, and P. St. J. Russell. Supercontinuum and four-wave mixing with q-switched pulses in endlessly single-mode photonic crystal fibres. *Opt. Express*, 12(2):299–309, 2004.

[64] J. K. Ranka, R. S. Windeler, and A. J. Stentz. Visible continuum generation in air-silica microstructure optical fibers with anomalous dispersion at 800 nm. *Opt. Letters*, 25(1):25–27, 2000.

[65] D. J. Jones, S. A. Diddams, J. K. Ranka, A. Stentz, R. S. Windeler, J. L. Hall, and S. T. Cundiff. Carrier-Envelope Phase Control of Femtosecond Mode-Locked Lasers and Direct Optical Frequency Synthesis. *Science*, 288(5466):635, 2000.

[66] T. Udem, R. Holzwarth, and T. W. Haensch. Optical frequency metrology. *Nature*, 416(6877):233–237, 2002.

[67] V. Tombelaine, P. Leproux, V. Couderc, and A. Barthlmy. Visible Supercontinuum Generation in Holey Fibers by Dual-Wavelength Subnanosecond Pumping. *Photonics Technology Letters, IEEE*, 18(23):2466–2468, 2006.

[68] C. Lesvigne, V. Couderc, A. Tonello, P. Leproux, A. Barthélémy, S. Lacroix, F. Druon, P. Blandin, M. Hanna, and P. Georges. Visible supercontinuum generation controlled by intermodal four-wave mixing in microstructured fiber. *Opt. Letters*, 32(15):2173–2175, 2007.

[69] C. Xiong, A. Witkowska, S. G. Leon-Saval, T. A. Birks, and W. J. Wadsworth. Enhanced visible continuum generation from a microchip 1064nm laser. *Opt. Express*, 14(13):6188–6193, 2006.

[70] A. Kudlinski, A. K. George, J. C. Knight, J. C. Travers, A. B. Rulkov, S. V. Popov, and J. R. Taylor. Zero-dispersion wavelength decreasing photonic crystal fibers for ultraviolet-extended supercontinuum generation. *Opt. Express*, 14(12):5715–5722, 2006.

[71] www.crystal-fibre.com.

[72] G. Ren, P. Shum, L. Zhang, X. Yu, W. Tong, and J. Luo. Low-loss all-solid photonic bandgap fiber. *Opt. Letters*, 32(9):1023–1025, 2007.

[73] T. A. Birks, F. Luan, G. J. Pearce, A. Wang, J. C Knight, and D. M. Bird. Bend loss in all-solid bandgap fibres. *Opt. Express*, 14(12):5688–5698, 2006.

[74] G. J. Pearce, T. D. Hedley, and D. M. Bird. Adaptive curvilinear coordinates in a plane-wave solution of maxwell's equations in photonic crystals. *Physical Review B (Condensed Matter and Materials Physics)*, 71(19):195108, 2005.

[75] A. Fuerbach, P. Steinvurzel, J. A. Bolger, A. Nulsen, and B. J. Eggleton. Nonlinear propagation effects in antiresonant high-index inclusion photonic crystal fibers. *Opt. letters*, 30(8):830–832, 2005.

[76] R. Jamier, N. Ducros, S. Février, M. E. Likhachev, and M. Salganskii. Tight control of the spectral broadening obtained by nonlinear conversion in a photonic bandgap fiber. In *Conference on Lasers and Electro-Optics/International Quantum Electronics Conference*, page JWA53. Optical Society of America, 2009.

[77] A. Btourn, A. Kudlinski, G. Bouwmans, A. Mussot, and Y. Quiquempois. Supercontinuum generation in solid-core photonic bandgap fibers. In *Conference on Lasers and Electro-Optics/Europe*, page CD8.4. Optical Society of America, 2009.

[78] S. V. Chernikov and P. V. Mamyshev. Femtosecond soliton propagation in fibers with slowly decreasing dispersion. *Journal of the Optical Society of America B: Optical Physics*, 8(8):1633–1641, 1991.

[79] S. V. Chernikov, E. M. Dianov, D. J. Richardson, and D. N. Payne. Soliton pulse compression in dispersion-decreasing fiber. *Opt. Letters*, 18(7):476–478, 1993.

[80] K. Smith and L. F. Mollenauer. Experimental observation of adiabatic compression and expansion of soliton pulses over long fiber paths. *Opt. Letters*, 14(14):751–753, 1989.

[81] www.fianium.com.

[82] www.koheras.com.

[83] M. L. V. Tse, P. Horak, J. H. V. Price, F. Poletti, F. He, and D. J. Richardson. Pulse compression at 1.06 μm in dispersion-decreasing holey fibers. *Opt. Letters*, 31(23):3504–3506, 2006.

[84] L. F. Mollenauer, R. H. Stolen, J. P. Gordon, and W. J. Tomlinson. Extreme picosecond pulse narrowing by means of soliton effect in single-mode optical fibers. *Opt. Letters*, 8(5):289–291, 1983.

[85] M. Foster, A. Gaeta, Q. Cao, and R. Trebino. Soliton-effect compression of supercontinuum to few-cycle durations in photonic nanowires. *Opt. Express*, 13(18):6848–6855, 2005.

[86] T. P. White, B. T. Kuhlmey, R. C. McPhedran, D. Maystre, G. Renversez, C. M. de Sterke, and L. C. Botten. Multipole method for microstructured optical fibers. I. Formulation. *Journal of the Optical Society of America B*, 19(10):2322–2330, 2002.

[87] B. T. Kuhlmey, T. P. White, G. Renversez, D. Maystre, L. C. Botten, C. M. de Sterke, and R. C. McPhedran. Multipole method for microstructured optical fibers. II. Implementation and results. *Journal of the Optical Society of America B*, 19(10):2331–2340, 2002.

[88] M. Tateda, N. Shibata, and S. Seikai. Interferometric method for chromatic dispersion measurement in a single-mode optical fiber. *Journal of Quantum Electronics, IEEE*, 17(3):404–407, 1981.

[89] P. V. Mamyshev, P. G. J. Wigley, J. Wilson, G. I. Stegeman, V. A. Semeonov, E. M. Dianov, and S. I. Miroshnichenko. Adiabatic compression of schrödinger solitons due to the combined perturbations of higher-order dispersion and delayed nonlinear response. *Phys. Rev. Lett.*, 71(1):73–76, Jul 1993.

[90] F. Gérôme, K. Cook, A. K. George, W. J. Wadsworth, and J. C. Knight. Delivery of sub-100fs pulses through 8m of hollow-core fiber using soliton compression. *Opt. Express*, 15(12):7126–7131, 2007.

[91] F. Gèrôme, P. Dupriez, J. Clowes, J. C. Knight, and W. J. Wadsworth. High power tunable femtosecond soliton sourceusing hollow-core photonic bandgap fiber, andits use for frequency doubling. *Opt. Express*, 16(4):2381–2386, 2008.

[92] N. Nishizawa and T. Goto. Characteristics of pulse trapping by ultrashort soliton pulse in optical fibers across zerodispersion wavelength. *Opt. Express*, 10(21):1151–1160, 2002.

[93] A. V. Gorbach, D. V. Skryabin, J. M. Stone, and J. C. Knight. Four-wave mixing of solitons with radiation and quasi-nondispersive wave packets at the short-wavelength edge of a supercontinuum. *Opt. Express*, 14(21):9854–9863, 2006.

[94] A. V. Gorbach and D. V. Skryabin. Light trapping in gravity-like potentials and expansion of supercontinuum spectra in photonic-crystal fibres. *Nature Photonics*, 1:653–657, 2007.

[95] N. Deguil, E. Mottay, F. Salin, P. Legros, and D. Choquet. Novel diode-pumped infrared tunable laser system for multi-photon microscopy. *Microscopy Research and Technique*, 63(1):23–26, 2004.

[96] G. McConnell. Confocal laser scanning fluorescence microscopy with a visible continuum source. *Opt. Express*, 12(13):2844–2850, 2004.

[97] K. Saitoh and M. Koshiba. Empirical relations for simple design of photonic crystal fibers. *Opt. Express*, 13(1):267–274, 2005.